JCI The Journal of Clinical Investigation

Inflammasome adaptor ASC promotes sustained neuroinflammation and mild cognitive impairment in a closed-head injury model

Tao Li, Sergio Castro-Gomez, Pablo Botella Lucena, Ana Vieira-Saecker, Stephanie Schwartz, Yingying Ding, Yushuang Deng, Maling Guo, Valentin Stein, Douglas T. Golenbock, Eicke Latz, Michael T. Heneka

J Clin Invest. 2026. https://doi.org/10.1172/JCI199818.

Research In-Press Preview **Inflammation** **Neuroscience**

Graphical abstract

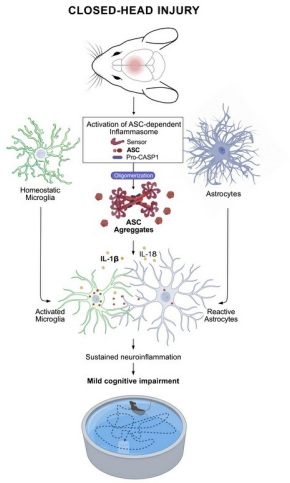

Inflammasome adaptor ASC promotes sustained neuroinflammation and mild cognitive impairment in a closed-head injury model

Tao Li*[1], Sergio Castro-Gomez*#[1,2], Pablo Botella Lucena[3], Ana Vieira-Saecker[1], Stephanie Schwartz[1,2], Yingying Ding[2], Yushuang Deng[4], Maling Gou[5], Valentin Stein[2], Douglas T. Golenbock[6], Eicke Latz[7,8,9], Michael T. Heneka#[3,6]

1. Clinic of Parkinson, Sleep and Movement Disorders, Center for Neurology, University Hospital Bonn, University of Bonn, Bonn, Germany
2. Institute of Physiology II, University Hospital Bonn, University of Bonn, Bonn, Germany
3. Luxembourg Centre for Systems Biomedicine (LCSB), University of Luxembourg, Belvaux, Luxembourg
4. German Center for Neurodegenerative Diseases (DZNE), Bonn, Germany
5. Department of Biotherapy, Cancer Center and State Key Laboratory of Biotherapy, West China Hospital, Sichuan University, Chengdu, PR China
6. Division of Infectious Diseases and Immunology, University of Massachusetts Medical School, Worcester, USA
7. Institute of Innate Immunity, University Hospital Bonn, Bonn, Germany
8. Centre of Molecular Inflammation Research, Norwegian University of Science and Technology, Trondheim, Norway
9. Deutsches Rheuma-Forschungszentrum (DRFZ), Berlin, Germany

*__Authorship notes:__ TL and SC-G contributed equally to this work.

#__Correspondence__: michael.heneka@uni.lu, sergio.castro-gomez@ukbonn.de

__Competing interests:__ M.T.H. is a scientific advisory board member at Alector the Dementia Discovery Fund, and Muna Therapeutics and has received honoraria for oral presentations from Pfizer, Novartis, Roche, Abbvie, and Biogen. E.L. is a co-founder and adviser at IFM Therapeutics, Dioscure Therapeutics, Stealth' Biotech, and Odyssey Therapeutics.

Abstract

Mild traumatic brain injury (mTBI) from closed-head injuries (CHI) can lead to prevalent neuropsychiatric disorders, including mood disorders and an increased risk for neurodegenerative diseases and dementia. Inflammasomes are molecular complexes crucial for neuroinflammation and secondary damage after trauma, however their role in mild CHI is poorly understood. In this study, we investigate the cellular expression of inflammasome-related genes and their functional significance in CHI models. Single-cell RNA sequencing analysis of cortical tissue after trauma revealed selective expression of *Asc* (also known as *Pycard*), which encodes the inflammasome adaptor Apoptosis-associated Speck-like protein containing a Caspase recruitment domain (ASC), predominantly in microglial clusters. Sustained upregulation of inflammasome-related proteins, microglia activation and astrocyte reactivity persisted up to 21 days in a model for mTBI, with this pattern significantly reduced in $Asc^{-/-}$ mice. Importantly, mild cognitive impairment induced after mild CHI was largely abrogated in $Asc^{-/-}$ mice. These findings suggest that ASC, as the primary inflammasome adaptor, plays a critical role in sustaining neuroinflammation and contributes to cognitive deficits after mild CHI. This study provides insights into the molecular neuroinflammatory mechanisms underlying CHI, potentially informing future therapeutic strategies.

Introduction

Traumatic brain injury (TBI) represents a significant global health challenge and is considered a silent epidemic, affecting individuals across all demographics and age groups. Every year, TBI affects around 1.5 million people in both the European Union (EU) and the United States (US). In the EU, these injuries are linked to about 57,000 deaths and 1.5 million hospital admissions (1), while in the US they cause roughly 50,000 deaths, 230,000 hospitalizations with survival, and 80,000–90,000 new cases of long-term disability (2). The majority of cases are clinically classified as mild TBI (mTBI), typically resulting from closed-head injuries (CHI) caused by falls, traffic accidents, violence, contact sports, or military actions (3, 4). Although mTBI symptoms can recover within days or weeks, up to 20% of individuals experience persistent physical, cognitive, and behavioral impairments that lead to a reduced quality of daily life and an elevated risk of neuropsychiatric disorders, including mood disorders and dementia (5–7). Despite its prevalence, the underlying pathophysiology of mTBI resulting from CHI remains poorly understood, posing great challenges for early clinical diagnosis and timely intervention.

Activated microglia and reactive astrocytes play crucial roles in innate immune responses and secondary damage following TBI. Prolonged activation of these cells impairs debris clearance, contributing to neuroinflammation, exacerbating neuronal dysfunction and damage, and promoting abnormal protein aggregation (8–10). Advances in imaging techniques have allowed the *in vivo* visualization of glial reactivity after CHI, emphasizing the involvement of microglia and astrocytes in the inflammatory cascade that contributes to the development of post-traumatic disorders (11–13). A key element in initiating and maintaining innate immune responses of the brain is inflammasome activation and signaling. Inflammasomes are oligomeric protein scaffolds rapidly activated by damage-associated molecular patterns (DAMPs), and organized as a tripartite complex: a cytosolic danger sensor such as the NLR family pyrin domain–containing protein 3 (NLRP3), a unique adaptor protein called Apoptosis-associated Speck-like protein containing a Caspase recruitment domain (ASC), and a proteolytic effector Caspase-1 (CASP1) (14). ASC, an intracellular adaptor protein common to almost all inflammasomes, oligomerizes into highly cross-linked macromolecular assemblies, forming visible ASC aggregates. The fibrillar ASC acts as a molecular platform to recruit pro-CASP1, which optimizes signal transduction via proximity-induced CASP1 activation. Activated CASP1 catalyzes the maturation of pro-forms of Interleukin-1β (IL-1β), IL-18, and mediates the proteolytic activation of Gasdermin D (GSDMD). Cleaved GSDMD oligomerizes and forms pores in the plasma membrane, allowing the release of IL-1β, IL-18, and other proinflammatory factors including ASC aggregates. The detection of tissue ASC ensembles is considered a typical hallmark of inflammasome activation (15). The activation of the inflammasome in CHI is likely driven by the well-described two-signal mechanism initiated by DAMPs released from injured or dying brain cells. The first signal involves priming, in which DAMPs are recognized by pattern recognition receptors (PRRs) such as Toll-like receptors (TLRs). This recognition activates the Nuclear Factor kappa-light-chain-enhancer of activated B-cells (NF-κB) pathway, leading to increased transcription of inflammasome genes, including *Nlrp3* and *Asc*. The second signal, or activation step, is triggered by various cellular stressors and further DAMPs generated during CHI. Key activators include potassium ion (K^+) efflux (16), mitochondrial

dysfunction with increased reactive oxygen species (ROS) production (17), extracellular ATP signaling via P2X7 receptors (18), and lysosomal disruption often resulting from phagocytosis of neuronal and myelin debris (19). Additional contributors include alterations in intracellular calcium levels, osmotic imbalances (20), and stress of organelles such as lysosomes (21) and endoplasmic reticulum (22), all converging to promote assembly of the inflammasome complex.

In humans, some inflammasome proteins are detected in blood and cerebrospinal fluid after TBI, and circulating levels of some proteins such as ASC and CASP1 have been proposed as biomarkers for determining injury severity (23–25). Furthermore, inflammasome activators, including NLRP1 (26), NLRP3 (27, 28), and absent in melanoma 2 (AIM2) (29), presumably contribute to the innate immune response and functional disability in mouse models of TBI. These studies primarily focused on inflammasome activation in models of moderate to severe TBI, such as the commonly used Controlled Cortical Impact (CCI), in which ASC has been hypothesized to be dispensable (30). At the same time, their contribution to mild CHI remains largely unexplored. In the present study, we hypothesized that ASC ensembles contribute actively to the secondary damage following CHI. We aimed to investigate their role in neuroinflammatory responses and subsequent cognitive functions by analyzing a well-established single-cell RNA sequencing (scRNA-seq) dataset of cortical cells from mice subjected to a CHI model (31) and by using an additional CHI mouse model that induces mild cognitive impairment (32). Our scRNA-seq data analysis reveals a subacute expression of *Asc* (also known as *Pycard*) in cortical cells from mice subjected to midline fluid percussion injury (mFPI), particularly in microglia subpopulations. In concordance with this analysis, we observed sustained upregulation of inflammasome-related proteins, including NLRP3, ASC, CASP-1, and IL-1β, following CHI, persisting up to 21 days post-injury (dpi). This expression pattern was significantly reduced in *Asc*$^{-/-}$ mice. Moreover, *Asc*$^{-/-}$ mice were protected from the mild cognitive impairment induced by our CHI model. We also observed ASC-dependent microglial and astrocytic reactivity and their cellular interactions that persist over time, accompanied by the upregulation, aggregation, and redistribution of the ASC protein. Our findings identify ASC, the primary inflammasome adaptor, as a key molecule in sustaining neuroinflammation and contributing to cognitive deficits after CHI.

Results

Subacute Asc expression in microglia subpopulations after CHI. To examine the cellular expression of gene coding for inflammasome-related proteins after CHI, our first approach was to adopt a single-cell transcriptomic analysis. We chose to re-examine a publicly available scRNA-seq dataset from dissociated cortical cells 7 days (7 days post injury, 7 dpi) following mFPI (31). mFPI mimics several relevant features of CHI including diffused trauma without localized lesion or hemorrhages, and closely models mild to moderate TBI (33). After quality control, we analyzed 14,688 control cells and 10,745 cells in the mFPI group (Figure 1A and supplemental Figure 1A). The complex multidimensional dataset was transformed and visualized using the nonlinear dimensionality reduction technique Uniform Manifold Approximation and Projection (UMAP) (Figure 1A, 1B, 1E). Examination of cellular transcriptional identities at the single-cell level uncovered 22 distinct cellular clusters. Cellular subpopulation labels were assigned via automated cell

type annotation per metadata sample using SingleR (34) (Supplemental Figure 1B). Cells identified as microglia were especially enriched in this dataset (Figure 1B). A differential expression gene analysis of this subset of cells showed a typical disease-associated microglia signature after TBI, with overexpression of type-1 interferon genes (such as *Ifi27l2a, Ifitm3, Ifit3, Irf7*) and *Apoe,* and reduction of homeostatic genes such as *tmem119* or *tgfb1* (Figure 1C).

We then evaluated, for each predicted cellular subpopulation, the expression of genes annotated to pathways related to inflammasome activation (pathcards.genecards.org (35), Supplemental Fig 1C). Notably, we found *Asc* as one of the genes with wider expression in clusters represented by microglia, macrophages, and other peripheral infiltrating immune cells (Figure 1D-E and Supplemental Figure 1C, 1D). These clusters showed a reduced percentage of cells expressing genes coding for inflammasome effectors such as *Gsdmd, Casp1, il1b* or *il18* (Figure 1D and E). Surprisingly, we found a very low percentage of cells expressing genes coding for inflammasome activators such as *Nlrc4, Nlrc5, Nlrp1b, Nlrp3 or Aim2* (Supplemental Fig 1C). These results suggest that the subacute and prolonged expression of the adaptor protein ASC, especially in microglia, may play a central role in the sustained innate immune response and pathophysiology of CHI.

ASC contributes to the sustained expression and processing of inflammasome mediators following mild CHI. To unveil the pathophysiological role of inflammasomes and specifically of ASC as main inflammasome adaptor and abundantly expressed gene in microglia after CHI, we adopted an electromagnetic CHI procedure as main model for mTBI (32). In this model, a controlled cortical impact injury is delivered directly to the midline surface of the skull using a 5 mm diameter tip at a specified depth and velocity (Supplemental Figure 2A). We found mild motor, reflex, or reaction deficits at 1- and 7 dpi when the mice were evaluated using the Revised Neurobehavioral Severity Scale (NSS-R) for rodents (36) (Supplemental Figure 2B). To examine the expression of inflammasome-related proteins after CHI, we performed immunoblot analysis of cortices from WT and *Asc*$^{-/-}$ mice that underwent either sham or CHI surgery. We analyzed and semi-quantified the protein levels of NLRP3, ASC, CASP1, and IL-1β at 1, 7, and 21 dpi (Figure 2A-I). Our results revealed sustained upregulation of these proteins up to 21 days after CHI in WT mice. Notably, mice with a constitutive genetic deficiency of the *Asc* gene (*Asc*$^{-/-}$) showed a significant deficit in the expression and cleavage of CASP1 (Figure 2D-E) and of IL-1β over time (Figure 2G) following CHI. ELISA measurements further demonstrated significantly lower soluble levels of IL-1β and TNF-α in *Asc*$^{-/-}$ mice (Figure 2H-I), particularly at later time points. We additionally evaluated the levels of cleavage of Caspase-8 (CASP8), a proposed non-canonical enzyme involved in IL-1β processing (37) (Supplemental Figure 2C and D), and its downstream effector Caspase-3 (CASP3), as indirect measurement of apoptotic pathways (38) (Supplemental Figure 2C and E). Consistent with the reduction in soluble IL-1β, *Asc*$^{-/-}$ cortices showed significantly reduced levels of cleaved CASP8 up to 21 days post CHI (Supplemental Figure 2D), which suggests parallel activation of canonical and non-canonical pathways of IL-1β processing, both of which appear largely dependent on ASC. Additionally, the cleavage of CASP3 was significantly reduced in *Asc*$^{-/-}$ mice (Supplemental Figure 2E), suggesting a strong neuroprotective effect and a complex crosstalk involving the activation of multiple types of cell death influenced by inflammasome signaling (39). Further

colocalization analysis of cleavage CASP3 immunostaining with the ionized calcium binding adaptor molecule 1 (Iba1$^+$) and Glial fibrillary acidic protein (GFAP$^+$) on cortices of WT mice revealed that cleaved CASP3 was predominantly localized in both the cytoplasm and nucleus of Iba1$^+$ cells, likely microglia, whereas its expression in GFAP$^+$, likely astrocytes, was comparatively weaker. These results suggest that CASP3 activation occurs in microglia or infiltrating macrophages, where it may participate in both apoptotic (nuclear) and non-apoptotic (cytoplasmic) signaling processes, consistent with its reported roles in regulating neuroinflammatory responses (40). Notably, microglia and astrocytes exhibiting stronger nuclear localization of cleaved CASP3 displayed neuroinflammatory morphological features, including nuclear condensation and cell body shrinkage (Supplemental Figure 2F and 2G).

To identify the cellular sources of IL-1β following mild CHI, we additionally conducted immunohistochemical staining for IL-1β, Iba1 and GFAP on cortices of WT mice in 7 and 21 dpi groups (Supplemental Figure 3A). At 7 days post-mTBI, IL-1β signal was found to be colocalized with or in the vicinity of GFAP$^+$ cells (presumably reactive astrocytes) and with Iba1$^+$ cells (likely microglia) (Supplemental Figure 3A). Interestingly, at 21 dpi, the majority of IL-1β was detected in Iba1$^+$ cells (microglia or infiltrating macrophages), suggesting a very active role of microglia in the TBI-dependent upregulation and secretion of this cytokine (Supplemental Figure 3B-C). Our findings thus emphasize the crucial role of inflammasome signaling, with ASC as the common adaptor protein, in sustaining the expression and processing of neuroinflammatory mediator after CHI. Moreover, we identified Iba1$^+$ cells, likely microglia, or infiltrating macrophages, as the primary cellular sources of IL-1β, especially at later time points post-injury.

ASC shapes the morphology of Iba1$^+$ cells following CHI. Microglia exhibit distinct adaptive morphologies in response to mechanical stimuli, and their morphology is considered a proxy for their function (41). To investigate microglia architecture after CHI, we performed immunofluorescence staining for Iba1 and skeleton analysis (42) to examine cell morphology in cortices of WT and *Asc*$^{-/-}$ mice at 1, 7, and 21 dpi (Figure 3A–B). First, we observed that *Asc*$^{-/-}$ mice consistently exhibited lower Iba1+ cell counts compared with WT mice at 7 dpi (Figure 3C), suggesting a decreased microgliosis in the subacute CHI phase. Next, we quantified the normalized changes in the morphology of Iba1$^+$ cells based on cell count. The morphological alterations, including the number of branches per cell, endpoints per cell, and branch length per cell, significantly decreased after injury in WT mice, particularly at 21 dpi. In contrast, *Asc*$^{-/-}$ mice showed a significant preservation of these morphological features at 21 dpi compared to WT mice (Figure 3D-F). In conclusion, our observations suggest a wave of microgliosis in the subacute phase and revealed a progressive debranching of Iba1$^+$ cells over time following injury. Notably, the lack of ASC demonstrated protection against these sustained cellular morphological alterations, particularly at later time points.

ASC regulates the reactivity of GFAP$^+$ cells following CHI. Previous studies have provided evidence that morphological changes in astrocytes are intricately linked to microglia activation during inflammation-induced responses (43). To examine reactive astrocytes and their morphological alterations following mild CHI, we performed a morphological analysis of GFAP$^+$ cells in contusional layers 1 and 2/3 of the retrosplenial and primary motor cortices, using the same method as for Iba1$^+$ cells (Figure 3G-H). We initially observed a noteworthy increase in the count of GFAP$^+$ cells at 1, 7, and 21 dpi in WT mice (Figure 3I),

confirming increased reactive astrogliosis in our model. *Asc* deficiency exerted a genotype-related effect in the cell count similar to what we observed in Iba1$^+$ cells, showing significantly lower numbers, especially at 7 dpi (Figure 3I). Subsequently, we quantified normalized morphological changes in GFAP$^+$ cells based on cell counts. The branches per cell, endpoints per cell, and length of branches per cell were significantly decreased after CHI, particularly at 21 dpi (Figure 3J–L). In contrast, *Asc*$^{-/-}$ mice showed preserved morphological features at 21 dpi compared to WT mice (Figure 3J–L). Interestingly, at 21 dpi, we observed clusters of aggregated GFAP$^+$ cells, indicating spatial reorganization post-injury. Similar morphological changes were evident in both microglia and reactive astrocytes after injury, suggesting a potential correlation or interactions between these two glial cell populations.

Iba1$^+$ and GFAP$^+$ cell interactions are modulated by ASC following CHI. To investigate the interactions between reactive astrocytes and microglia in the contusional cortex following injury, we performed surface–surface colocalization analysis of the contact areas after 3D reconstruction of confocal images from GFAP- and Iba1-immunostained tissues (Figure 4A). We observed a significant increase in contact area between reactive astrocytes and microglia at 7 dpi, reaching a peak at 21 dpi in WT mice (Figure 4B). Notably, the contact area was significantly reduced at 7 and 21 dpi in *Asc*$^{-/-}$ mice (Figure 4B), which may be explained by the deficient microglia activation and reactive astrogliosis observed in our previous analysis. These findings, together with our expression analysis, suggest that inflammasome ensembles and neuroinflammatory processing are essential for sustained microglial and astrocytic responses and cellular interactions after mild CHI.

Genetic deficiency in the Asc gene provides protection against mild cognitive impairment following mild CHI. Having demonstrated that *Asc* is predominantly expressed by microglia subpopulations in the subacute phase of CHI, contributing to the sustained inflammasome activation, as well as microglial and astrocytic reactivity following CHI, we next sought to investigate whether the genetic removal of the main inflammasome adaptor protein ASC influences cognitive outcomes after mild CHI. In humans, a significant number of individuals present transient or persistent cognitive impairment following mTBI, including deficits in memory recall, procedural tasks, executive functions, attention and emotional symptoms such as heightened anxiety (44). To investigate the role of ASC in neurobehavioral phenotypes following mild CHI, we conducted a comprehensive battery of behavioral tests evaluating motor, emotional, and cognitive functions (Figure 5A). Motor coordination and balance were assessed using the rotarod task from 4 days before until 3 dpi. Anxiety-related and exploratory behaviors were measured by the elevated O-maze (EOM) and open field (OF) tests at 5 and 7 dpi, respectively. Nest building behavior test (NBT), a sensitive indicator of motivation and stress, was evaluated 1 day before and at 1, 3, and 7 dpi. Short-term spatial memory was examined with the novel object location memory (OLM) test at 7 and 8 dpi. Furthermore, the Morris Water Maze (MWM), a more cognitively demanding paradigm, was performed from 10 to 20 dpi, including a spatial learning phase (10–15 dpi), a 24-hour long-term memory test (16 dpi), and a cued learning phase (17–20 dpi) to assess procedural learning and sensorimotor function (Figure 5A and 6A).

Our mCHI protocol did not induce impairments in latency to fall (Figure 5B) or running speed (Supplemental Figure 4A) in the rotarod test, nor in exploratory frequency (Figure 5C and Supplemental Figure 4B) or

stretch-attend postures in the open sectors (Figure 5D) of the EOM, or in total path length in the OF (Figure 5E). Injured WT and *Asc*$^{-/-}$ mice showed no significant increase in the percentage of time spent in the center (Figure 5F) or in locomotor velocity in the OF (Supplemental Figure 4C). Although mCHI induced transient deficits in nest building at 1 and 3 dpi, no differences were observed between WT and *Asc*$^{-/-}$ mice at any assessed time point (Figure 5G).

At 8 and 9 dpi, experimental groups underwent the OLM test to assess short-term spatial memory. Mice were trained for two consecutive days with three identical objects placed in a box containing visual cues on the walls. We observed no differences in the exploration frequency of three identical objects during the training phase across experimental groups (Supplemental Figure 4D). One hour after the last training session, one object was relocated to a novel position. Mice naturally explored the displaced object significantly longer. mCHI significantly impaired both exploration frequency (Figure 5H) and the preference index in the OLM test in WT mice (Figure 5I). These deficits were absent in *Asc*$^{-/-}$ mice subjected to mCHI (Figure 5H-I), indicating a preserved short-term spatial memory.

During MWM (Figure 6A), WT mice subjected to mCHI exhibited a comparable daily reduction in path length toward the hidden platform comparable to WT sham animals (Figure 6B-C). However, CHI significantly increased thigmotaxis, reflected by prolonged swimming near the pool walls during the learning phase in WT injured mice (Figure 6D-E). In the cued version of the task, WT injured mice similarly demonstrated a daily reduction in path length (Figure 6F-G), increased thigmotactic behavior (Figure 6H-I). This procedural deficit was significantly reduced in *Asc*$^{-/-}$ mice (Figure 6D-E and 6H-I). Moreover, *Asc*$^{-/-}$ mice displayed preserved long-term spatial memory 24 hours after the learning phase, as visually suggested by the density plots (heat maps) of swim paths (Figure 6J). This observation was further supported by a significantly greater percentage of time spent exploring the target quadrant (Figure 6K), and by more frequent crossings over the virtual target platform compared to control quadrants or platforms during the probe trial at 16 dpi (Figure 6L). Furthermore, *Asc*$^{-/-}$ mice showed slightly higher velocity on the last day of cued learning (Supplemental Figure 4E and F). Collectively, these data show that CHI induces mild cognitive impairments, mainly as procedural and memory deficits in the OLM and the MWM tests, which appear to be largely dependent on ASC expression.

NLRP3 regulates ASC aggregation and distribution following CHI. The NLRP3 is widely recognized as one of the most relevant inflammasome activators in the context of TBI, with growing evidence indicating its central role in mediating neuroinflammation and secondary brain damage (45, 46). To explore the involvement NLRP3 in the aggregation of ASC as the main inflammasome adaptor in post-CHI, we conducted immunohistochemical staining of the contusional cortical tissue for Iba1, GFAP, and ASC at 7 and 21 dpi in WT and *Nlrp3*$^{-/-}$ mice (Figure 7A). We used a KO-validated monoclonal antibody for ASC detection (Supplemental Figure 5A-B). 3D surface reconstruction of Iba1, GFAP and ASC immunosignal analysis was subsequently conducted (Figure 7A and Supplemental Figure 5C). We detected a significant increase in the total number of fluorescent ASC aggregates, especially in Iba1^{+} cells (likely microglia) at 7 dpi similar to the mRNA expression of *Asc* observed in the scRNA-Seq data analysis following mFPI (Figure 1B, Figure 7B and Supplemental Figure 5D). The number of ASC aggregates within Iba1^{+} cells followed the

total ASC aggregates pattern (Figure 7B and Supplemental Figure 5C-D). Notably, *Nlrp3*$^{-/-}$ injured mice showed comparable ASC aggregates counts, both overall and within Iba1^{+} cells, compared to WT mice (Figure 7B), but significantly lower aggregates in GFAP^{+} cells (presumably reactive astrocytes, Figure 7C). Interestingly, at 21 dpi, the number of ASC aggregates outside Iba1^{+} and GFAP^{+} cells (extra-glia ASC) significantly increased in both WT and *Nlrp3*$^{-/-}$ mice (Figure 7D). However, this ensembles count was significantly lower in *Nlrp3*$^{-/-}$ mice compared to WT controls (Figure 7D). Additionally, as ASC aggregates numbers increased within microglia, their corresponding volumes also increased. To further analyze ASC aggregation, we categorized ASC aggregates by volume (1–20 μm^3, 20–30 μm^3, 30–40 μm^3) and quantified the number of ensembles in each category (Figure 7E and Supplemental Figure 5E-F). ASC aggregates within a range of 30–40 μm^3 were significantly decreased in the *Nlrp3*$^{-/-}$ mice at 21 dpi (Figure 7E). Collectively, our findings demonstrate a remarkable upregulation of ASC aggregates outside of Iba1^{+} and GFAP^{+} cells, along with significant ASC aggregation at 21 dpi. *Nlrp3*$^{-/-}$ mice displayed reduced ASC aggregation within Iba1^{+} cells and fewer extra-glia ASC aggregates compared to WT group at 21 dpi. These observations highlight the essential role of NLRP3 not only in promoting inflammasome activation after brain injury but also in facilitating ASC aggregation, as previously suggested in *in-vitro* studies (47).

Interaction between reactive astrocytes and microglia correlates with ASC distribution following CHI. To further investigate the relationship between reactive astrocytes and microglia interactions and ASC distribution following CHI, we conducted correlation analysis between ASC aggregates and glial contact areas after 3D reconstruction (Figure 7F–I). Notably, we observed a strong positive correlation between the cell contact area and the number of extra-glia ASC aggregates *($r = 0.86$, $p < 0.0001$)* (Figure 7G) as well as ASC aggregates within GFAP^{+} cells *($r = 0.93$, $p < 0.0001$)* (Figure 7I), in WT animals after CHI. Although lower correlation coefficients were found between the reactive astrocytes and microglia contact areas and the number of ASC aggregates in microglia *($r = 0.73$, $p < 0.0001$)* (Figure 7H) and the overall count of ASC aggregates *($r = 0.82$, $p < 0.0001$)* (Figure 7F), these correlations remained significantly positive (Figure 7F–I). Interestingly, the genetic deficiency of *Nlrp3* significantly reduced the correlation between the contact area and the number of extra-glia ASC aggregates *($z = 1.95$, $p < 0.05$)* (Figure 7G) as well as ASC in GFAP^{+} cells *($z = 2.54$, $p < 0.01$)* (Figure 7I). In summary, these results indicate that ASC aggregation after CHI is partly dependent on NLRP3 and additionally reactive astrocytes and microglia contacts are influenced by ASC expression, distribution, and aggregation, especially the ASC aggregates located outside of Iba1^{+} and GFAP^{+} cells.

Discussion

In this study, we identify *Asc* as a key gene expressed in monocytes, macrophages, and especially in microglia populations during the subacute phase of CHI based on scRNA-seq data from mouse cortical cells after mFPI. Sustained ASC protein expression in our mild CHI model was observed predominantly in Iba1^{+} cells (presumably microglia) and, to a lesser extent, in GFAP^{+} cells (likely reactive astrocytes). We demonstrated that *Asc*$^{-/-}$ mice exhibited attenuated neuroinflammatory responses and improved cognitive performance after mTBI, supporting an ASC-dependent regulation of microglial and astrocyte reactivity and

innate immune responses that contribute to neurobehavioral deficits following mTBI. Our findings not only complement and expand previous preclinical and clinical studies on moderate to severe TBI models (48, 49), which highlight the role of inflammasome cascades and their critical involvement in regulating secondary inflammatory responses after TBI, but also demonstrate that the main inflammasome adaptor protein ASC is a key element in neuroinflammatory responses and cognitive impairment following mTBI. In contrast to several studies on moderate-to-severe TBI models, where the expression of inflammasome-related proteins typically peaks within the initial week following injury and declines over time (28, 50, 51), we found a progressive and sustained increase in inflammasome-related proteins especially after the first 7 days following mild CHI. This temporal pattern aligns with our observations of sustained morphological changes of reactive astrocytes and microglia during a later phase (21 dpi). These discrepancies across experimental models and TBI severities indicate that inflammasome activation within innate immune responses and tissue repair processes depends on the extent of injury. Furthermore, the sustained proinflammatory profiles of activated microglia and reactive astrocytes imply that both glial cell types contribute to the propagation of inflammation through inflammasome-associated pathways after injury. In our study, we observed that, compared to injured WT mice, the number of $Iba1^+$ cells remained stable in *Asc*$^{-/-}$ mice at both 7- and 21 dpi, indicating attenuated microglial and macrophage turnover following trauma (Figure 3C and I). WT mice, in contrast, exhibited a distinct peak of $Iba1^+$ cell proliferation and activation at 7 dpi, concurrent with the subacute neuroinflammatory response characteristic of the CHI model (42). By 21 dpi, $Iba1^+$ cell density in WT mice declined toward baseline, likely reflecting ASC-dependent CASP1–mediated pyroptotic cell death and subsequent release of proinflammatory mediators, including IL-1β and extracellular ASC aggregates. Following this microglia peak, astrocytes displayed prominent reactive morphology at 21 dpi relative to 7 dpi, possibly driven by the continued activation of neurotoxic astrocytes through microglial inflammasome signaling in response to ongoing tissue damage, as previously described in stress paradigms (52). Furthermore, these findings align with existing evidence suggesting that distinct glial cell types respond differentially to brain injury in a temporal sequence (42, 53–55). Future studies should address the contribution of ASC-mediated neuroinflammation during the chronic phases of TBI (beyond 30 dpi). Notably, a recent study using a unilateral closed cortical impact model reported that Iba1 and GFAP immunoreactivity peak at 21 dpi. While Iba1 immunoreactivity returned to baseline by 40 dpi, GFAP reactivity persisted, suggesting a longer astrocytic response throughout the chronic phase (56). Previous studies have reported that CHI elicits astrocyte reactivity through JAK/STAT3- and NF-κB–dependent signaling pathways, leading to cytoskeletal remodeling, GFAP induction, and cytokine release that support both repair and inflammation during the acute and subacute phases of injury (55, 57). Moreover, astrocytes can respond to microglia-derived factors such as IL-1α, TNF-α, and C1q, which promote distinct reactive phenotypes with predominantly pro-inflammatory features (43). In the chronic phase, proliferating reactive astrocytes from perilesional regions could migrate toward the lesion core to contribute to glial scar formation and wound processes. This scarring response may help contain inflammation and protect surrounding tissue but can also impede axonal regeneration and neural recovery (57).

We additionally observed a widespread upregulation of inflammasome components following CHI, particularly at 21 dpi, with a significant increase in the cleaved forms of CASP1, CASP8, and IL-1β. Our results suggest the involvement of several ASC-dependent inflammasomes in the inflammatory pathways after CHI. This is evident by the pronounced reduction in CASP1, CASP3 and CASP8 levels and morphological changes in microglia and reactive astrocytes observed in *Asc*$^{-/-}$ mice. Most notably, our behavioral evaluation during the late subacute phases shows that short-term spatial memory, anxiety-related behaviors (thigmotaxis), mild procedural learning deficits and long-term memory impairments were significantly diminished in animals with genetic deficiency of the *Asc* gene (Figures 5 and 6). Furthermore, we identified a significant positive correlation between astrocyte–microglia interactions and the number of ASC aggregates. Consistent with previous work, extracellular ASC appears to facilitate the propagation of inflammatory mediators such as IL-1β and TNF-α following inflammasome activation (15, 58). These cytokines not only promote the aggregation of glia and infiltrated cells around the trauma epicenter (59, 60), but may also influence cell communication far from the lesion site through extracellular ASC. Given its prion-like properties (58), ASC can spread to neighboring glial cells and trigger secondary activation of the ASC-mediated inflammasome cascade, as previously demonstrated in Alzheimer's disease (AD)-related amyloidosis (61, 62). Collectively, these observations support a central role of ASC in maintaining neuroinflammation and glial reactivity after CHI.

Strikingly, *Nlrp3*$^{-/-}$ mice exhibited fewer ASC aggregates outside Iba1^{+} and GFAP^{+} cells, with a significant reduction of ASC inclusions within GFAP^{+} cells (bona fide astrocytes) but not within Iba1^{+} cells (Figure 7). This finding may reflect the constitutive abundance of ASC in microglia and a cell type–specific regulation of inflammasome activation during neuroinflammatory responses. Recent studies have emphasized distinct inflammasome repertoires in glial subtypes. Microglia predominantly engage canonical inflammasome pathways, expressing and activating multiple complexes—including NLRP1 (63), NLRP3 (46, 51, 64), NLRC4 (65), and AIM2 (66)—depending on the nature of injury and DAMPs involved. Upon activation, microglial inflammasomes promote CASP1 cleavage and robust IL-1β secretion, intensifying secondary neuroinflammatory cascades and neuronal damage. In contrast, astrocytes express lower basal levels of inflammasome components and appear to rely predominantly on NLRP3 for inflammasome assembly and inflammatory signaling following TBI. Astrocytic NLRP3 expression can be upregulated by microglia-derived cytokines (67, 68) or extracellular ATP released from damaged cells (69), leading to moderate CASP1 activation and IL-1β/IL-18 maturation, thereby sustaining reactive gliosis. Conditional NLRP3 deletion in astrocytes attenuates CASP1 activation and depression-like behavior after mild TBI, supporting a cell type–specific dependence on NLRP3 in astrocytes (70). Accordingly, the reduced ASC aggregation observed in astrocytes of *Nlrp3*$^{-/-}$ mice likely reflects their predominant reliance on NLRP3 for inflammasome assembly. In contrast, microglia can engage alternative inflammasome pathways (e.g., NLRP1, NLRC4, AIM2) that mediate ASC speck formation independently of NLRP3. Alternatively, diminished NLRP3 activity in microglia may reduce extracellular ASC aggregates release and intercellular propagation, further limiting secondary glial activation.

Our findings, however, contrast with a previous report on moderate CCI, where *Asc*$^{-/-}$ mice showed no differences in motor recovery or volume lesions (30). This inconsistency may suggest that, in the context of low-grade chronic neuroinflammation induced by mild, uncontrolled stimuli, such as a single concussion event, the expression, oligomerization, and propagation of ASC may occur gradually compared to the high-grade neuroinflammation triggered by severe injuries. Similarly, ASC-dependent inflammasome activation and pathological protein aggregation have been observed in several neurodegenerative disorders characterized by sustained chronic low-grade neuroinflammation (71), such as Alzheimer's and Parkinson's disease, where ASC plays a decisive role in the aggregating and further propagating Amyloid β (61) and α-Synuclein (72). Considering our findings, ASC may participate in immune mechanisms that potentially predispose to neurodegenerative processes following TBI (73). Nonetheless, future investigations are still required to establish a comprehensive understanding of the specific temporal participation of inflammasomes across varying injuries severities and risk factors for neurodegeneration.

There are several limitations that warrant consideration in our study. While we focused on the expression of inflammasome mediators and associated cellular morphology, these parameters may not fully reflect the intricate interplay between compensatory mechanisms operating within affected neuronal networks or the broader anti-inflammatory modulation of secondary immune responses. Furthermore, although our scRNA-seq analysis identified specific cellular clusters upregulating *Asc* during the subacute phase of the CHI model, the use of a conventional global knockout line limits our ability to delineate the distinct contributions of peripheral and central cell populations to the post-injury immune response.

Future research should aim to delineate the longitudinal neuroinflammatory trajectory across defined neural, glial, and peripheral cellular compartments, particularly using inducible knockout models and pharmacological interventions targeting ASC aggregation or inflammasome assembly. In this context, recently developed orally bioavailable NLRP3 inhibitors have shown beneficial effects on neurological recovery, ASC aggregation, and microglial morphology after moderate CCI (46). Moreover, humanized monoclonal antibodies such as IC100 (74) and single-domain antibodies targeting ASC (75) have demonstrated preclinical efficacy in other inflammatory conditions, supporting their potential translational relevance to target ASC and ASC-dependent inflammasome signaling in clinical trials of TBI.

Our findings pave the way to delve into specific pharmacological agents that can effectively modulate ASC expression, activity and aggregation, and assess their impact on neurological outcomes after TBI. Considering our findings, pharmacological interventions targeting ASC may help to mitigate neuroinflammation and potentially promote neuroprotection, enhancing recovery of injury and preventing further neurodegeneration and disability.

Methods

Sex as a biological variable. Sex was not considered as a biological variable.

Ethical compliance. We followed the European guidelines for animal research, conformed to the requirements of the German Animal Welfare Act and received approval from North Rhine-Westphalia State

Agency for Nature, Environment and Consumer Protection under folder number 81-02.04.2019.A026 and 2024-791-Grundantrag.

Mice. Male and female mice (approximately 50% of each sex), aged 6–7 months, on a mixed C57BL/6 background (C57BL/6N-J), were used in all experiments. All animals were bred and housed in the House of the Experimental Medicine at the University Hospital Bonn in Germany. WT, *Nlrp3*$^{-/-}$, and *Asc*$^{-/-}$ mice were initially sourced from Millennium Pharmaceuticals as previously published (76). All mice were backcrossed with C57BL/6N mice and maintained under pathogen-free, standardized conditions with a 12:12-hour light/dark cycle and ad libitum access to food and water. Behavioral experiments were conducted during the dark phase of the light/dark cycle.

Electromagnetic controlled closed-head injury model of mild traumatic brain injury. To model mild TBI in mice**,** we adapted the electromagnetic controlled Closed-Head Model previously described (77) (Supplemental Figure 2A). Briefly, mice were anesthetized with 5% isoflurane during induction, and 1.5-2% isoflurane mixed with 100% oxygen (0.5-1 L/min) during surgery and fixed in a stereotaxic frame (Stoelting, Dublin, Ireland). A 1-mL latex pipette bulb filled with water was placed under the head to distribute the impact force. A midline sagittal scalp incision was made, and a single controlled midline skull impact was delivered at coordinates 0.0 mm mediolateral and -1.5 mm anteroposterior, with a velocity of 5 m/s, dwell time of 100 ms, and impact depth of 1.0 mm, using a stereotaxic electromagnetic impactor with a 5.0-mm steel tip (Stereotaxic Impactor, Leica Biosystems, Germany). Sham mice underwent identical surgical procedures without impact injury. In the post-operative phase, mice received carprofen (5 mg/kg) subcutaneously once daily and tramadol (1 mg/mL) in drinking water for three days.

Revised Neurobehavioral Severity Scale (NSS-R). NSS-R consists of a structured series of neurological tests evaluating motor and sensory abilities, including assessments of general mobility, reflex inhibition, and postural control (36). Scores range from 0, indicating normal function, to 20, representing the most severe impairment.

Rotarod test. Motor coordination and balance were assessed using an accelerating rotarod apparatus (Ugo-Basile, Gemonio, Italy). The rotation speed progressively increased from 5 to 40 revolutions per minute over a 5-minute testing period. Mice underwent three trials daily for four consecutive days prior to CHI, followed by two additional testing sessions after the injury. The latency to fall and the rotational speed at the time of fall were automatically recorded by the system for each trial.

Nest building behavior test (NBT). The NBT was employed to assess natural, species-typical behaviors indicative of daily functional capacities. Individual mice were housed alone and provided with standardized nesting material in their home cages at the beginning of their active dark cycle. Mice were given 12 hours to construct nests, after which nest quality was evaluated. Nest scoring utilized a validated scale from 1 to 5, considering factors such as structure, coherence, and completeness of the nests, thereby quantifying functional nesting performance (78).

Elevated O Maze (EOM). Anxiety-related behavior and risk evaluation were measured using an EOM apparatus composed of a circular elevated runway (46 cm diameter, 5.5 cm width) positioned 40 cm above the ground. The maze featured two enclosed arms alternating with two open sectors.

Open Field Test (OF). Voluntary locomotion and exploratory activity were examined in a 50 cm cubic open field chamber constructed from opaque gray acrylic. Mice were recorded for 15 minutes per session, under low indirect lighting conditions (~40 lux).

Novel Object Location Memory (OLM) Test. The OLM assay was performed within the open field arena with visual cues on one of the walls, with the floor covered in a 1-cm layer of used and smell-saturated bedding material. Following a 1-day habituation period where mice explored the arena with three identical colored Lego objects (2 × 4 cm) placed in fixed positions for 5 minutes daily, the test day began with a 6-minute exploration of these objects. Object investigation time was tracked automatically by Noldus EthoVision software (Wageningen, Netherlands). After a 1-hour delay, one object was relocated to a new position while the other two remained stationary. The animals were reintroduced for a 5-minute session to assess preference for the displaced object. The Discrimination Index (%) was calculated during the initial 3 minutes as: [Time exploring relocated object / Total exploration time of all objects] × 100.

Morris water maze (MWM). The evaluation of spatial learning and memory was conducted between 10 and 20 dpi. A circular pool with a diameter of 1 m was filled with white opacified water maintained at a temperature of 21–23 °C. The pool was dimly lit (approximately 40 lx) and surrounded by a white curtain. Asymmetrically placed distal cues were positioned on the pool wall to serve as spatial references. The pool was virtually divided into four quadrants, one of which contained a hidden platform (15 cm in diameter) submerged 1.5 cm below the water surface. Mice were trained to locate the platform using the distal cues for orientation. Training consisted of four trials per day for five consecutive days. During each trial, mice were placed into the water facing the pool wall in a quasi-randomized order to prevent them from developing fixed strategies. Mice were given 60 s to find the platform; if they failed to locate it within this time, they were manually guided to it. Once on the platform, mice were allowed to remain there for 15 s before the next trial began. After completing all four trials for the day, mice were dried and returned to their home cages. The integrated time or distance traveled during these trials was analyzed. A spatial probe trial was conducted 24 hours after the final training session (16 dpi). For this test, the hidden platform was removed, and mice were allowed to swim freely for 60 s. The drop position was in the quadrant opposite where the platform had been located, with each mouse facing the wall at the center of that quadrant. One day after the spatial probe trial, a visually cued learning phase began. During this phase, the platform was flagged for visibility and relocated to a different quadrant, while all distal cues were removed. Mice underwent three trials per day for three consecutive days (17–20 dpi) to learn to locate the flagged platform. All mouse movements were recorded and tracked using Noldus EthoVision software (Wageningen, Netherlands).

Tissue preparation. Mice were deeply anesthetized using ketamine (100 mg/kg) and xylazine (20 mg/kg) and transcardially perfused with at least 30 ml of ice-cold PBS at designated time points (Sham, 1, 7, and 21 dpi). Following perfusion, brains were carefully dissected. One hemisphere was snap-frozen in liquid nitrogen and stored at -80 °C until biochemical analyses, while the other hemisphere was fixed in 4% paraformaldehyde overnight. Coronal brain sections (40 µm thick) were obtained using a Leica VT1000S vibratome (Leica Microsystems Inc.) from the region spanning bregma -0.45 to -1.85 mm. Sections were collected in PBS at intervals of 300 µm for various staining procedures.

Primary antibodies. For immunoblotting, the following primary antibodies were used: mouse anti-CASP1 from (1:1000; AdipoGen; AG-20B-0042), rabbit anti-ASC (1:1500; Cell Signaling; D2W8U), rabbit anti-NLRP3 (1:500; Cell Signaling; D4D8T), rabbit anti-IL-1β from (1:1000; E7V2A; Cell Signaling), rabbit anti-CASP3 (1:1000; D3E9; Cell Signaling), and rabbit anti-CASP8 (1:1000; D5B2; Cell Signaling). For immunohistochemical analysis, the antibodies included rabbit anti-Iba1 from (1:1000; Fujifilm Wako reagents, 019-19741), goat anti-Iba1 (1:1000; Abcam; EPR16588), rat anti-GFAP (1:300; ThermoFisher; 2.2B10), goat anti-IL-1β (1:500; R&D Systems; AF-401-SP), rabbit anti-ASC (1:1500; Cell Signaling; D2W8U) and rabbit anti-CASP3 (1:1000; D3E9; Cell Signaling).

Tissue protein extraction and immunoblotting. After thawing, brain tissue was homogenized in PBS containing 1 mM EDTA, 1 mM EGTA, and protease inhibitor cocktail Halt™ (Thermo Scientific, Waltham, Massachusetts, U.S.). The homogenates were extracted in RIPA buffer [25 mM Tris–HCl (pH 7.5), 150 mM NaCl, 1% Nonidet P-40, 0.5% NaDOC, 0.1% SDS] and centrifuged at 20000 ×g for 30 minutes. RIPA fractions were separated using NuPAGE® electrophoresis gels (Thermo Scientific, Waltham, Massachusetts, USA) and immunoblotted with primary antibodies, followed by incubation with the corresponding secondary antibodies. Immunoreactivity was detected with an Odyssey CLx Imaging System (LI-COR, Bad Homburg, Germany), and images were analyzed using ImageJ (NIH, Bethesda, USA).

ELISA pro-inflammatory cytokine panel. The levels of IL-1β and TNF-α in RIPA fractions were measured using the V-PLEX Plus Mouse Pro-Inflammatory Panel 1 (Meso Scale Discovery, Rockville, USA), following the manufacturer's protocol. Samples were diluted 1:1 on the plate with the reagent diluent provided in the kit. Signals were detected using a QuickPlex SQ 120 plate reader (Meso Scale Discovery, Rockville, USA).

Immunohistochemistry. Brain sections were washed three times for 5 min with PBS and incubated in citrate buffer for 5 min at 95°C. After antigen retrieval, the sections were cooled down at room temperature and washed with PBS and in 0.5% Triton X-100 B (PBS-T), then blocked for 1 h with 1% BSA in PBS-T and incubated overnight with the primary antibodies. Next, the sections were washed three times for 5 min in PBS-T, incubated with appropriate secondary antibodies (1:1000) for 60 min, and following with three times with PBS washing for 5 min. The tissue was mounted using ProLong™ Gold Antifade Mountant with DNA Stain DAPI (Thermo Scientific, Waltham, Massachusetts, U.S.). Three coronal brain sections per animal (between bregma −1.00 mm and −1.85 mm) were selected. Confocal z-stack images of the contusion were primarily acquired from layers 1 and 2/3 of the retrosplenial and primary motor cortex. Each z-stack consisted of 10 optical slices (c × z × t = 10), with one frame captured per acquisition. Imaging parameters were standardized across all samples: the pixel size was set to 0.1559814 µm in both the x and y axes, and the voxel depth (z-step) was maintained at 2.0 µm.

Skeleton analysis of microglia and reactive astrocytes. Morphological changes in microglia and reactive astrocytes were quantitatively analyzed using a skeleton analysis method (79). Images were imported into ImageJ software (Bethesda, Maryland, USA), converted to grayscale, and adjusted for brightness and contrast to enhance cell process visibility. After obtaining binary images of microglia and reactive astrocytes, we used the plugin skeletonize to obtain skeletons, representing the medial axis of cell processes. Morphological parameters measured included: Process Branches, defined as number of branching points.

Endpoints, defined as number of terminal points. Process Lengths, defined as total length of all processes. The data were normalized by dividing the measurements by the number of cells in each image.

Contact analysis between microglia and reactive astrocytes. Imaris Image Analysis Software (version 9.5, Oxford Instruments, Oxon, England) was used to analyze the contact area between microglial and astrocytic surfaces. 3D reconstructions were created using the tool surfaces by setting intensity thresholds to differentiate cell surfaces from the background. Adjustments were made to ensure accurate cell boundary representation. The Surface-Surface Contact X-Tension identified and analyzed overlapping regions between microglial and astrocytic surfaces, generating a new surface to represent the contact area. The contact area (μm^2) was calculated based on the number of overlapping voxels within the 3D reconstructions.

Analysis of ASC aggregates. The cortical impact area was examined using a confocal LSM900 microscope (Zeiss, Oberkochen, Baden-Württemberg, Germany). Images were captured under consistent confocal settings and processed with Imaris Image Analysis Software (Oxford Instruments, Oxon, England) to identify ASC aggregates. Standardized settings were maintained across samples, including pinhole size, laser intensity, digital gain, and offset. Z-stacks were collected to obtain the complete 3D structure of cells and ASC aggregates. Image preprocessing included adjusting brightness and contrast, reducing noise, and subtracting background to enhance aggregate visibility. Imaris Image Analysis Software was used to create 3D reconstructions of microglia, astrocytes, and ASC aggregates. The "Surfaces" tool generated accurate 3D models by setting intensity thresholds. The Spots tool identified and quantified ASC aggregates based on fluorescence intensity and size, with thresholds set using positive (mCherry-ASC mice) and negative (*Asc*$^{-/-}$ mice) controls. The Spots Close to Surface tool analyzed the spatial distribution of ASC aggregates relative to microglia or astrocytes, indicating potential inflammasome activation.

IL-1β analysis. Co-immunostainings for IL-1β, Iba1 and GFAP were performed at 7 and 21 dpi. Three-dimensional reconstructions of microglia, reactive astrocytes, neuronal nuclei, and IL-1β signals were generated using Imaris Image Analysis Software (Oxford Instruments, Oxon, UK). The "Spots" tool quantified IL-1β signals in the 3D space by analyzing fluorescence intensity and particle size thresholds. To assess spatial relationships, the "Spots Close to Surface" tool measured the proximity of IL-1β signals to cellular surfaces, evaluating potential associations with microglia, astrocytes, or neurons. Quantitative metrics, including the number of IL-1β spots adjacent to specific cell types, were measured for statistical analysis.

Single-cell RNA-sequencing data analysis. Raw FASTQ files and count matrices are publicly available in the NCBI GEO database under accession number GSE160763 (31). Single-cell RNA-seq data were analyzed using Seurat v5.1.0 in R v4.3.2 (80). Briefly, cells with over 5000 detected genes, UMI counts under 12,500, and less than 1% mitochondrial gene content were retained, followed by log-transformation of the data. We selected the top 4000 highly variable genes for principal component analysis (PCA) and used the top 20 principal components as input for UMAP dimensionality reduction. Cell cycle states were determined using Seurat's CellCycleScoring (81) function with marker genes from Tirosh *et al.* (80). Batch correction was performed using Harmony to integrate datasets across samples (82). Clusters were identified at a resolution of 0.5. Cellular identities were assigned via automated cell type annotation using SingleR

(34), which assigns cellular identity for single cell transcriptomes by comparison to reference data sets of pure cell types sequenced by microarray or RNA-sequencing (RNA-seq). Annotation relied on a reference dataset of 358 mouse RNA-seq samples annotated to 18 major cell types (83). Figures were generated using Tidyverse (84), SCpubr (85), and Enhanced Volcano (86).

Statistics and reproducibility. Data other than scRNA-seq were analyzed using GraphPad Prism Software version 9.0 or later (GraphPad Software, Inc., La Jolla, CA, USA) and are presented as mean ± SEM. Immunohistochemical quantifications and behavioral analyses were performed by investigators blinded to genotype and experimental condition. After assessing the distribution, statistical comparisons were performed using either a two-tailed t-test or one- or two-way ANOVA with Bonferroni's or Tukey's post hoc test to identify group differences. Morris Water Maze (MWM) learning data were analyzed using repeated-measures two-way ANOVA with Tukey's post hoc test. Correlation analyses were performed using non-parametric Spearman correlations. Differences between Spearman correlation coefficients were assessed using the standard Fisher's z-transformation and subsequent comparison (87). Results were considered statistically significant at $p < 0.05$.

Data availability. Values for all data points in graphs are reported in the Supporting Data Values file. Sequencing analysis was performed on previously published, publicly available data (31). Raw FASTQ files and count matrices are available in the NCBI GEO database (GSE160763).

Code availability. Code used in analyzing scRNA-seq data is available at https://gitlab.lcsb.uni.lu/pablo.botellalucena/rna_single_seq.

Author contributions

Conceptualization: SCG, MTH. Methodology: ASV, PBL, SCG, TL, SS, YD, MG. Investigation: ASV, PBL, SCG, TL, SS, YDi, YDe. Funding acquisition: SCG, MTH. Supervision: SCG, MTH. Writing of original draft: SCG, TL, YD. Writing, review, and editing: MTH, SCG, PB, TL, YDi, YDe, VS, EL

Funding support

- Alzheimer Forschung Initiative e.V (Grant 21060 to SCG)
- Hertie Network of Excellence in Clinical Neuroscience (Grant 2021-1A-12 to SCG)
- Deutsche Forschungsgemeinschaft (DFG) - Neuro-aCSis – Bonn Neuroscience Clinician Scientist Programm (Project 493623632 to SCG)
- DFG – ImmunoSensation^2 (EXC2151–390873048 to SCG and MTH).
- National Strategy for Translational Projects for Gene and Cell Therapy Products and Associated Diagnostics from the Federal Ministry of Education and Research (BMBF, Grant 01_BIH_TP_2410 to SCG).
- Fonds National de la Recherche within the PEARL program (FNR/16745220 to MTH and PBL).

- China Scholarship Council (CSC, File No. 202308310126 to YDi and File No. 201908510162 to YDe).
- Academic Program Department of Biotherapy Cancer Center and State Key Laboratory of Biotherapy, West China Hospital, Sichuan University to TL und MG.

Acknowledgements

We thank Christina Ising and Ildikó Rácz for their support in obtaining approval from the local ethics committee for the animal experiments; Sean-Patrick Riechers for assistance with editing the final draft; Paula Martorell, Nadia Villacampa, and Juan Ignacio Muñoz Manco for valuable discussions; Dorit Glass and Isabel Blaumeuser for technical assistance; the DZNE Light Microscopy Facility for support with imaging and analysis; and all members of the Heneka and Stein laboratories for their valuable discussions and support.

Address correspondence to: Michael T. Heneka, Luxembourg Centre for Systems Biomedicine, University of Luxembourg, 6 Avenue du Swing, 4367 Belvaux, Luxembourg. Phone: +352 621 712 820; Email: michael.heneka@uni.lu. Or to: Sergio Castro-Gomez, Clinic of Parkinson, Sleep and Movement Disorders, Center for Neurology, University Hospital Bonn, University of Bonn, Venusberg-Campus 1, 53127 Bonn, Germany. Phone: +49 228 287 53217; Email: sergio.castro-gomez@ukbonn.de.

References

1. Maas AIR, et al. Traumatic brain injury: integrated approaches to improve prevention, clinical care, and research. *The Lancet Neurology*. 2017;16(12):987–1048.

2. Thurman DJ, et al. Traumatic Brain Injury in the United States: A Public Health Perspective: *Journal of Head Trauma Rehabilitation*. 1999;14(6):602–615.

3. Cassidy JD, et al. Incidence, risk factors and prevention of mild traumatic brain injury: results of the who collaborating centre task force on mild traumatic brain injury. *Journal of Rehabilitation Medicine*. 2004;36(0):28–60.

4. Naumenko Y, et al. Mild traumatic brain injury as a pathological process. *Heliyon*. 2023;9(7):e18342.

5. Rathbone ATL, et al. A review of the neuro- and systemic inflammatory responses in post concussion symptoms: Introduction of the “post-inflammatory brain syndrome” PIBS. *Brain Behav Immun*. 2015;46:1–16.

6. Ahman S, et al. Long-term follow-up of patients with mild traumatic brain injury: a mixed-method study. *J Rehabil Med*. 2013;45(8):758–764.

7. Déry J, et al. Prognostic factors for persistent symptoms in adults with mild traumatic brain injury: an overview of systematic reviews. *Syst Rev*. 2023;12(1):127.

8. Burda JE, Bernstein AM, Sofroniew MV. Astrocyte roles in traumatic brain injury. *Exp Neurol*. 2016;275 Pt 3(0 3):305–315.

9. Loane DJ, Kumar A. Microglia in the TBI brain: The good, the bad, and the dysregulated. *Exp Neurol*. 2016;275 Pt 3(0 3):316–327.

10. Simon DW, et al. The far-reaching scope of neuroinflammation after traumatic brain injury. *Nat Rev Neurol*. 2017;13(9):572.

11. Perez-Polo JR, et al. Inflammatory consequences in a rodent model of mild traumatic brain injury. *J Neurotrauma*. 2013;30(9):727–740.

12. Weil ZM, Gaier KR, Karelina K. Injury timing alters metabolic, inflammatory and functional outcomes following repeated mild traumatic brain injury. *Neurobiol Dis*. 2014;70:108–116.

13. Lv W, et al. mTBI-Induced Systemic Vascular Dysfunction in a Mouse mTBI Model. *Brain Sci*. 2022;12(2):232.

14. Ravichandran KA, Heneka MT. Inflammasomes in neurological disorders - mechanisms and therapeutic potential. *Nat Rev Neurol*. 2024;20(2):67–83.

15. Franklin BS, Latz E, Schmidt FI. The intra- and extracellular functions of ASC specks. *Immunol Rev*. 2018;281(1):74–87.

16. Tapia-Abellán A, et al. Sensing low intracellular potassium by NLRP3 results in a stable open structure that promotes inflammasome activation. *Sci Adv*. 2021;7(38):eabf4468.

17. Zhou R, et al. A role for mitochondria in NLRP3 inflammasome activation. *Nature*. 2011;469(7329):221–225.

18. Karmakar M, et al. Neutrophil P2X7 receptors mediate NLRP3 inflammasome-dependent IL-1β secretion in response to ATP. *Nat Commun*. 2016;7:10555.

19. Aflaki E, et al. Lysosomal storage and impaired autophagy lead to inflammasome activation in Gaucher macrophages. *Aging Cell*. 2016;15(1):77–88.

20. Gong T, et al. Orchestration of NLRP3 Inflammasome Activation by Ion Fluxes. *Trends in Immunology*. 2018;39(5):393–406.

21. Katsnelson MA, et al. NLRP3 inflammasome signaling is activated by low-level lysosome disruption but inhibited by extensive lysosome disruption: roles for K+ efflux and Ca2+ influx. *Am J Physiol Cell Physiol*. 2016;311(1):C83–C100.

22. Kang H, et al. ER-to-lysosome Ca2+ refilling followed by K+ efflux-coupled store-operated Ca2+ entry in inflammasome activation and metabolic inflammation. *eLife*. 2024;12:RP87561.

23. Pérez-Bárcena J, et al. Serum Caspase-1 as an Independent Prognostic Factor in Traumatic Brain Injured Patients. *Neurocrit Care*. 2022;36(2):527–535.

24. Kerr N, et al. Inflammasome proteins as biomarkers of traumatic brain injury. *PLoS One*. 2018;13(12):e0210128.

25. Eagle SR, et al. Impact of obese body mass index on inflammasome blood biomarkers and neurocognitive performance following traumatic brain injury with Glasgow coma scale 13 to 15. *J Neurol Sci*. 2024;464:123159.

26. de Rivero Vaccari JP, et al. Therapeutic neutralization of the NLRP1 inflammasome reduces the innate immune response and improves histopathology after traumatic brain injury. *J Cereb Blood Flow Metab*. 2009;29(7):1251–1261.

27. Irrera N, et al. Lack of the Nlrp3 Inflammasome Improves Mice Recovery Following Traumatic Brain Injury. *Front Pharmacol*. 2017;8:459.

28. Liu H-D, et al. Expression of the NLRP3 inflammasome in cerebral cortex after traumatic brain injury in a rat model. *Neurochem Res*. 2013;38(10):2072–2083.

29. Adamczak SE, et al. Pyroptotic neuronal cell death mediated by the AIM2 inflammasome. *J Cereb Blood Flow Metab*. 2014;34(4):621–629.

30. Brickler T, et al. Nonessential Role for the NLRP1 Inflammasome Complex in a Murine Model of Traumatic Brain Injury. *Mediators of Inflammation*. 2016;2016:1–11.

31. Witcher KG, et al. Traumatic Brain Injury Causes Chronic Cortical Inflammation and Neuronal Dysfunction Mediated by Microglia. *J Neurosci*. 2021;41(7):1597–1616.

32. Macheda T, Roberts K, Bachstetter AD. Electromagnetic Controlled Closed-Head Model of Mild Traumatic Brain Injury in Mice. *JoVE*. 2022;(187):64556.

33. Lifshitz J, et al. Clinical relevance of midline fluid percussion brain injury: Acute deficits, chronic morbidities and the utility of biomarkers. *Brain Inj*. 2016;30(11):1293–1301.

34. Aran D, et al. Reference-based analysis of lung single-cell sequencing reveals a transitional profibrotic macrophage. *Nat Immunol*. 2019;20(2):163–172.

35. Belinky F, et al. PathCards: multi-source consolidation of human biological pathways. *Database (Oxford)*. 2015;2015:bav006.

36. Yarnell AM, et al. The Revised Neurobehavioral Severity Scale (NSS-R) for Rodents. *Curr Protoc Neurosci*. 2016;75:9.52.1-9.52.16.

37. Antonopoulos C, et al. Caspase-8 as an Effector and Regulator of NLRP3 Inflammasome Signaling. *Journal of Biological Chemistry*. 2015;290(33):20167–20184.

38. Clark RS, et al. Caspase-3 mediated neuronal death after traumatic brain injury in rats. *J Neurochem*. 2000;74(2):740–753.

39. Bertheloot D, Latz E, Franklin BS. Necroptosis, pyroptosis and apoptosis: an intricate game of cell death. *Cell Mol Immunol*. 2021;18(5):1106–1121.

40. McKenzie BA, et al. Activation of the executioner caspases-3 and -7 promotes microglial pyroptosis in models of multiple sclerosis. *J Neuroinflammation*. 2020;17(1):253.

41. Green TRF, Rowe RK. Quantifying microglial morphology: an insight into function. *Clinical and Experimental Immunology*. 2024;216(3):221–229.

42. Morrison H, et al. Quantitative microglia analyses reveal diverse morphologic responses in the rat cortex after diffuse brain injury. *Sci Rep*. 2017;7(1):13211.

43. Liddelow SA, et al. Neurotoxic reactive astrocytes are induced by activated microglia. *Nature*. 2017;541(7638):481–487.

44. McCauley SR, et al. Patterns of Early Emotional and Neuropsychological Sequelae after Mild Traumatic Brain Injury. *Journal of Neurotrauma*. 2014;31(10):914–925.

45. Chakraborty R, Tabassum H, Parvez S. NLRP3 inflammasome in traumatic brain injury: Its implication in the disease pathophysiology and potential as a therapeutic target. *Life Sci*. 2023;314:121352.

46. Castro-Gomez S, et al. NLRP3 inhibition maintains microglia architecture and enhances behavioral recovery after traumatic brain injury. *bioRxiv*. [published online ahead of print: 2025]. https://doi.org/10.1101/2025.06.25.660862.

47. Hochheiser IV, et al. Directionality of PYD filament growth determined by the transition of NLRP3 nucleation seeds to ASC elongation. *Sci Adv*. 2022;8(19):eabn7583.

48. Hu X, et al. Role of Pyroptosis in Traumatic Brain and Spinal Cord Injuries. *Int J Biol Sci*. 2020;16(12):2042–2050.

49. Mortezaee K, et al. Inflammasome: Its role in traumatic brain and spinal cord injury. *J Cell Physiol*. 2018;233(7):5160–5169.

50. Dempsey C, et al. Inhibiting the NLRP3 inflammasome with MCC950 promotes non-phlogistic clearance of amyloid-β and cognitive function in APP/PS1 mice. *Brain Behav Immun*. 2017;61:306–316.

51. Xu X, et al. Selective NLRP3 inflammasome inhibitor reduces neuroinflammation and improves long-term neurological outcomes in a murine model of traumatic brain injury. *Neurobiology of Disease*. 2018;117:15–27.

52. Li S, et al. Microglial NLRP3 inflammasome activates neurotoxic astrocytes in depression-like mice. *Cell Rep*. 2022;41(4):111532.

53. Witcher KG, et al. Traumatic brain injury-induced neuronal damage in the somatosensory cortex causes formation of rod-shaped microglia that promote astrogliosis and persistent neuroinflammation. *Glia*. 2018;66(12):2719–2736.

54. Susarla BTS, et al. Temporal Patterns of Cortical Proliferation of Glial Cell Populations after Traumatic Brain Injury in Mice. *ASN Neuro*. 2014;6(3):AN20130034.

55. Nespoli E, et al. Glial cells react to closed head injury in a distinct and spatiotemporally orchestrated manner. *Sci Rep*. 2024;14(1):2441.

56. Alkaslasi MR, et al. The transcriptional response of cortical neurons to concussion reveals divergent fates after injury. *Nat Commun*. 2025;16(1):1097.

57. Sawant N, et al. Incomplete accumulation of perilesional reactive astrocytes exacerbates wound healing after closed-head injury by increasing inflammation and BBB disruption. *Experimental Neurology*. 2024;374:114700.

751 58. Franklin BS, et al. The adaptor ASC has extracellular and “prionoid” activities that propagate
752 inflammation. *Nat Immunol*. 2014;15(8):727–737.

753 59. Sofroniew MV. Molecular dissection of reactive astrogliosis and glial scar formation. *Trends Neurosci*.
754 2009;32(12):638–647.

755 60. Wang H, et al. Portrait of glial scar in neurological diseases. *Int J Immunopathol Pharmacol*.
756 2018;31:2058738418801406.

757 61. Venegas C, et al. Microglia-derived ASC specks cross-seed amyloid-β in Alzheimer’s disease. *Nature*.
758 2017;552(7685):355–361.

759 62. Friker LL, et al. β-Amyloid Clustering around ASC Fibrils Boosts Its Toxicity in Microglia. *Cell Rep*.
760 2020;30(11):3743-3754.e6.

761 63. Liu H, et al. Pro-inflammatory and proliferative microglia drive progression of glioblastoma. *Cell Rep*.
762 2021;36(11):109718.

763 64. Heneka MT, et al. NLRP3 is activated in Alzheimer’s disease and contributes to pathology in APP/PS1
764 mice. *Nature*. 2013;493(7434):674–678.

765 65. Poh L, et al. Evidence that NLRC4 inflammasome mediates apoptotic and pyroptotic microglial death
766 following ischemic stroke. *Brain, Behavior, and Immunity*. 2019;75:34–47.

767 66. Ye L, et al. Conditional knockout of AIM2 in microglia ameliorates synaptic plasticity and spatial
768 memory deficits in a mouse model of Alzheimer’s disease. *CNS Neurosci Ther*. 2024;30(6):e14555.

769 67. He M, et al. NLRP3/Caspase-1-Mediated Pyroptosis of Astrocytes Induced by Antipsychotics Is
770 Inhibited by a Histamine H1 Receptor-Selective Agonist. *Front Aging Neurosci*. 2022;14:847561.

771 68. She N, et al. NLRP3 inflammasome regulates astrocyte transformation in brain injury induced by
772 chronic intermittent hypoxia. *BMC Neurosci*. 2022;23(1):70.

69. Albalawi F, et al. The P2X7 Receptor Primes IL-1β and the NLRP3 Inflammasome in Astrocytes Exposed to Mechanical Strain. *Front Cell Neurosci*. 2017;11:227.

70. Miao H-T, et al. Astrocytic NLRP3 cKO mitigates depression-like behaviors induced by mild TBI in mice. *Neurobiol Dis*. 2025;205:106785.

71. Castro-Gomez S, Heneka MT. Innate immune activation in neurodegenerative diseases. *Immunity*. 2024;57(4):790–814.

72. Zheng R, et al. ASC specks exacerbate α-synuclein pathology via amplifying NLRP3 inflammasome activities. *J Neuroinflammation*. 2023;20(1):26.

73. Graham A, et al. Mild Traumatic Brain Injuries and Future Risk of Developing Alzheimer's Disease: Systematic Review and Meta-Analysis. *JAD*. 2022;87(3):969–979.

74. Desu HL, et al. IC100: a novel anti-ASC monoclonal antibody improves functional outcomes in an animal model of multiple sclerosis. *J Neuroinflammation*. 2020;17(1):143.

75. Bertheloot D, et al. Nanobodies dismantle post-pyroptotic ASC specks and counteract inflammation in vivo. *EMBO Mol Med*. 2022;14(6):e15415.

76. Kanneganti T-D, et al. Bacterial RNA and small antiviral compounds activate caspase-1 through cryopyrin/Nalp3. *Nature*. 2006;440(7081):233–236.

77. Macheda T, Roberts K, Bachstetter AD. Electromagnetic Controlled Closed-Head Model of Mild Traumatic Brain Injury in Mice. *J Vis Exp*. [published online ahead of print: September 28, 2022];(187). https://doi.org/10.3791/64556.

78. Deacon RM. Assessing nest building in mice. *Nat Protoc*. 2006;1(3):1117–1119.

79. Young K, Morrison H. Quantifying Microglia Morphology from Photomicrographs of Immunohistochemistry Prepared Tissue Using ImageJ. *JoVE*. 2018;(136):57648.

80. Tirosh I, et al. Dissecting the multicellular ecosystem of metastatic melanoma by single-cell RNA-seq. *Science*. 2016;352(6282):189–196.

81. Watson S, et al. Modification of Seurat v4 for the Development of a Phase Assignment Tool Able to Distinguish between G2 and Mitotic Cells. *Int J Mol Sci*. 2024;25(9):4589.

82. Sun N, et al. Human microglial state dynamics in Alzheimer's disease progression. *Cell*. 2023;186(20):4386-4403.e29.

83. Benayoun BA, et al. Remodeling of epigenome and transcriptome landscapes with aging in mice reveals widespread induction of inflammatory responses. *Genome Res*. 2019;29(4):697–709.

84. Wickham H, et al. Welcome to the Tidyverse. *JOSS*. 2019;4(43):1686.

85. Blanco-Carmona E. Generating publication ready visualizations for Single Cell transcriptomics using SCpubr. *bioRxiv*. [published online ahead of print: 2022]. https://doi.org/10.1101/2022.02.28.482303.

86. Blighe K, Rana S, Lewis M. EnhancedVolcano: Publication-ready volcano plots with enhanced colouring and labeling. [published online ahead of print: 2018]. https://github.com/kevinblighe/EnhancedVolcano.

87. Lenhard W, Lenhard A. Hypothesis Tests for Comparing Correlations. *Psychometrica*. [published online ahead of print: 2014]. https://doi.org/10.13140/RG.2.1.2954.1367.

813 **Graphical abstract**

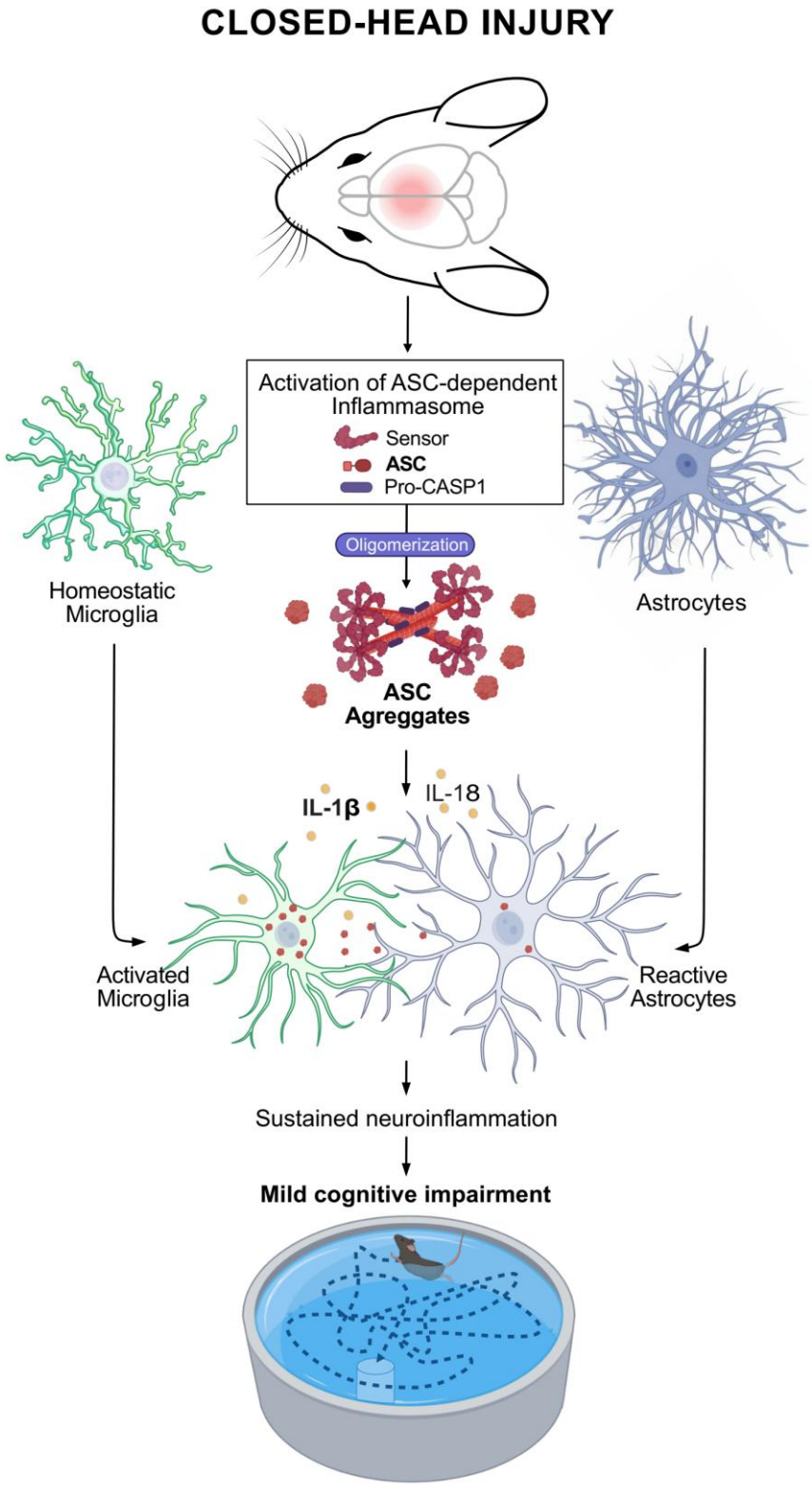

814

Figure 1: Subacute *Asc* expression in microglia after a model for CHI.

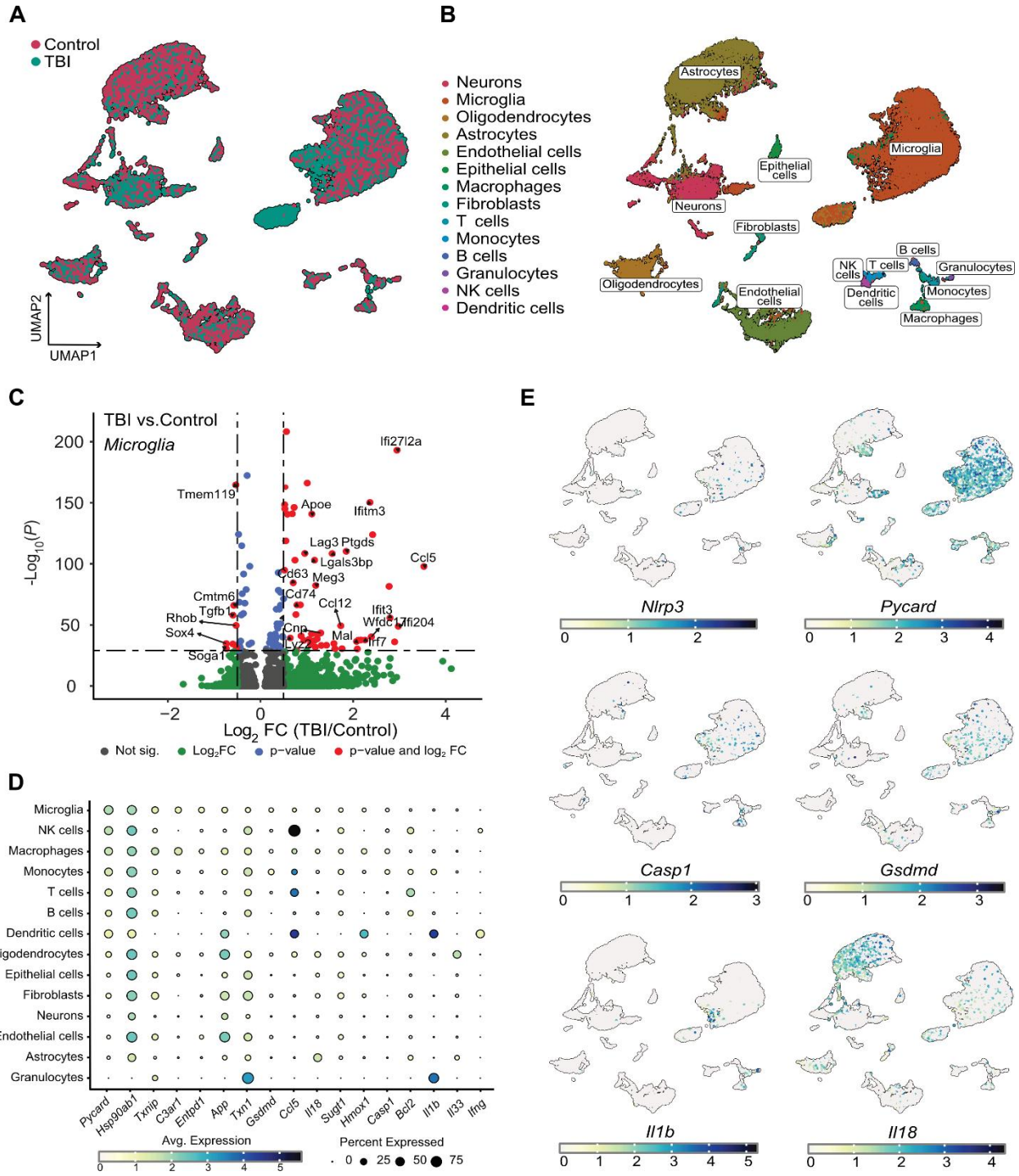

(**A-B**). Single-cell RNA sequencing (scRNA-seq) analysis of brain suspended cells from mice 7 days after mFPI. **A.** UMAP visualization shows clustering of different cell populations, with mFPI and control samples overlaid. **B.** Annotated cell types, including microglia, macrophages, and other immune and neural cells after cluster identification. **C.** Volcano plot depicting differentially expressed genes in microglia of control

and mFPI samples. **D.** Dot plot expression analysis showing percent of cells expressing key inflammasome-related genes across various brain cell types, highlighting *Asc* expression in microglia, Natural Killer (NK) cells, macrophages, and monocytes. **E.** UMAP projection of colored cells relative to the expression of canonical inflammasome-related genes *Nlrp3*, *Pycard (Asc)*, *Casp1, Il1b, Il18 and Gsdmd*.

Figure 2: **ASC contributes to the upregulation of inflammasome mediators following CHI.**

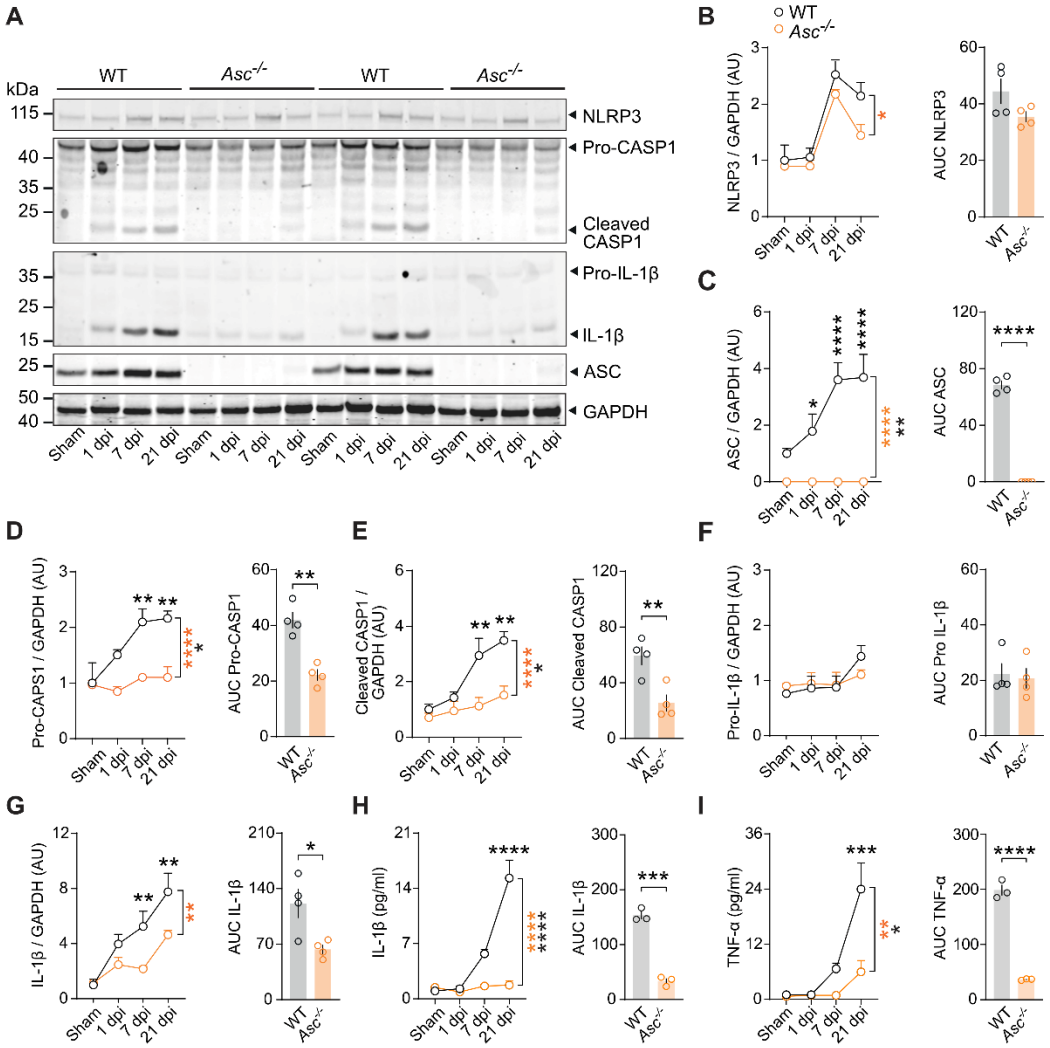

A. Immunoblot detection and **B-G.** densitometric semi-quantification of inflammasome-related proteins NLRP3, ASC, Caspase-1 (CASP1), IL-1β at 1, 7, and 21 dpi in contusional cortices from WT and *Asc*$^{-/-}$ mice following Sham or CHI. (left panels $n = 4$ per group and time point, $^{*}p < 0.05$, $^{**}p < 0.01$, $^{***}p < 0.001$, $^{****}p < 0.0001$, Ordinary two-way ANOVA, Bonferroni's test. AU, arbitrary units. **H, I.** Levels of IL-1β and TNF-α in brain lysates from WT and *Asc*$^{-/-}$ mice at 1, 7, and 21 dpi following CHI. $n = 3$ - 4 per group and time point, Left panels represent ordinary two-way ANOVA, Bonferroni's test, $^{*}p < 0.05$, $^{**}p < 0.01$, $^{***}p < 0.001$. Right panels in **B-I** represent integrated relative concentrations (Area Under Curve, AUC), $^{**}p < 0.01$, $^{***}p < 0.001$ by Student's t-test. dpi, days post-injury.

Figure 3: Morphology of Iba1⁺ and GFAP⁺ cells are modulated by ASC following CHI.

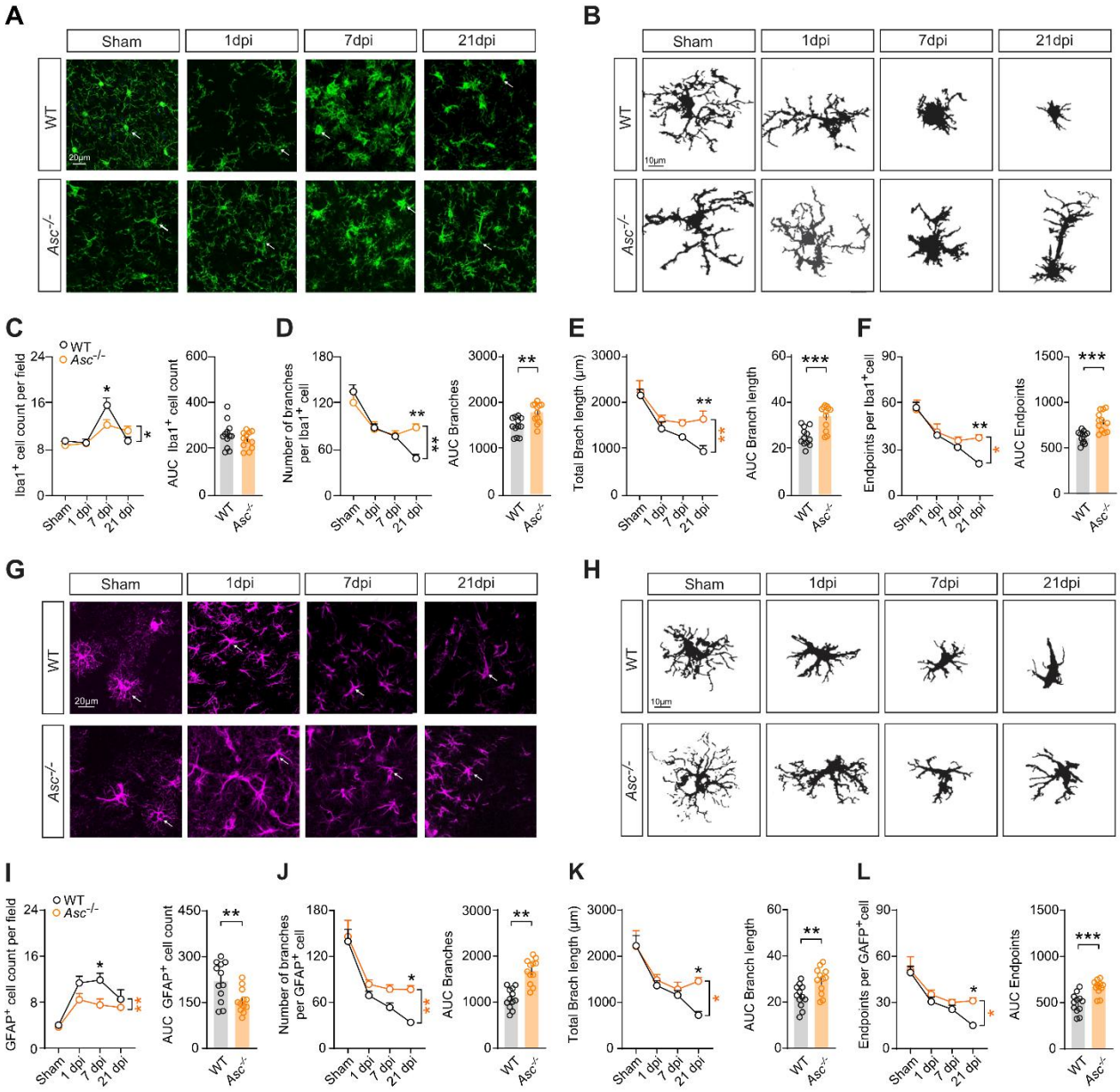

A. Immunohistochemistry of Iba1 (green, presumably microglia) in cortices from WT, and *Asc*$^{-/-}$ mice at Sham, 1, 7, and 21 dpi following CHI. Arrows indicate representative morphological changes. Scale bar, 20 μm. **B.** Representative skeletonized Iba1⁺ cells following CHI. Scale bars, 10 μm. Quantitative analysis of **C.** Iba1⁺ cell counts; **D.** branch numbers per cell, **E.** total branch length per cell and **F.** endpoint numbers per cell at 1, 7, and 21 dpi in WT and *Asc*$^{-/-}$ mice subjected to sham or CHI. **G.** Immunohistochemistry of GFAP (magenta, presumably astrocytes) in cortices from WT and *Asc*$^{-/-}$ mice at 1, 7, and 21 dpi following CHI. Arrows indicate representative morphological changes. Scale bar, 20 μm. **H.** Representative skeletonized GFAP⁺ cells following CHI. Scale bars, 10 μm. Quantitative analysis of **I.** GFAP⁺ cell counts;

J. branch numbers per cell, **K.** total branch length per cell and **L.** endpoint numbers per cell at 1, 7, and 21 dpi in WT and *Asc*$^{-/-}$ mice subjected to sham or CHI. n = 12 slices from 4 mice per group per each time point, *p < 0.05, ***p < 0.01, ***p < 0.001, ****p < 0.0001 by ordinary two-way ANOVA with Bonferroni's post hoc test. Right panels show integrative AUC of each marker over time (dpi). *p < 0.05, **p < 0.01, ***p < 0.001, ****p < 0.0001 by Student's t-test.

Figure 4: Cellular interactions of microglia and reactive astrocytes are modulated by ASC following CHI.

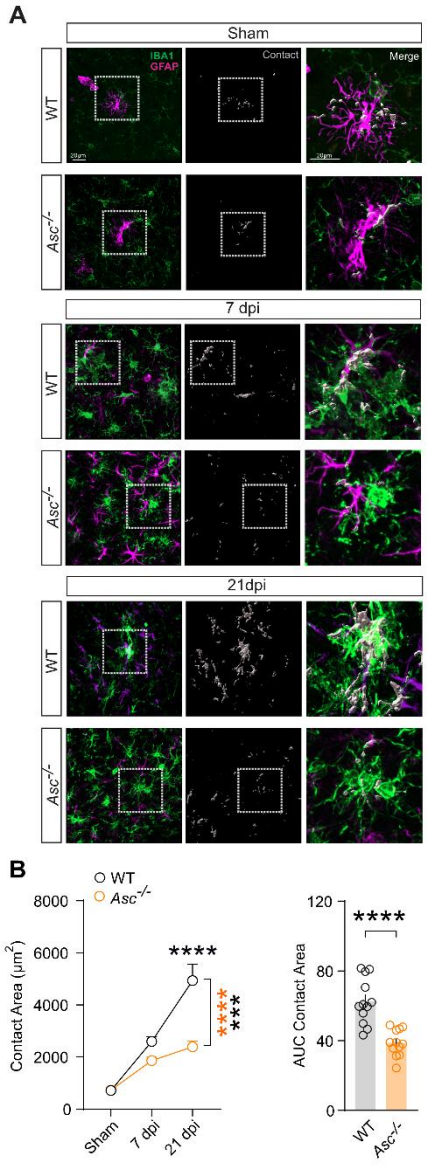

A. Immunohistochemistry for Iba1 (green) and GFAP (magenta) in cortices of WT and *Asc*$^{-/-}$ mice at Sham, 7 and 21 dpi. Surface-surface colocalization analysis after 3D reconstruction was used to estimate contact areas between Iba1^{+} cells and GFAP^{+} cells. Rectangles highlight examples of glial surface-surface colocalization, shown in high magnification views. Scale bar, 20 μm. **B.** Quantification of contact areas between Iba1^{+} cells and GFAP^{+} cells at 7 and 21 dpi in WT, and *Asc*$^{-/-}$ mice subjected to Sham or CHI. n = 12 slices from 4 mice per group per each time point, *p < 0.05, ***p < 0.01, ***p < 0.001, ****p < 0.0001 by ordinary two-way ANOVA with Bonferroni's post hoc test. Right panels show integrative AUC of each marker over time (dpi). *p < 0.05, **p < 0.01, ***p < 0.001, ****p < 0.0001 by Student's t-test.

Figure 5: *Asc*$^{-/-}$ mice show preserved short-term spatial memory following mild CHI.

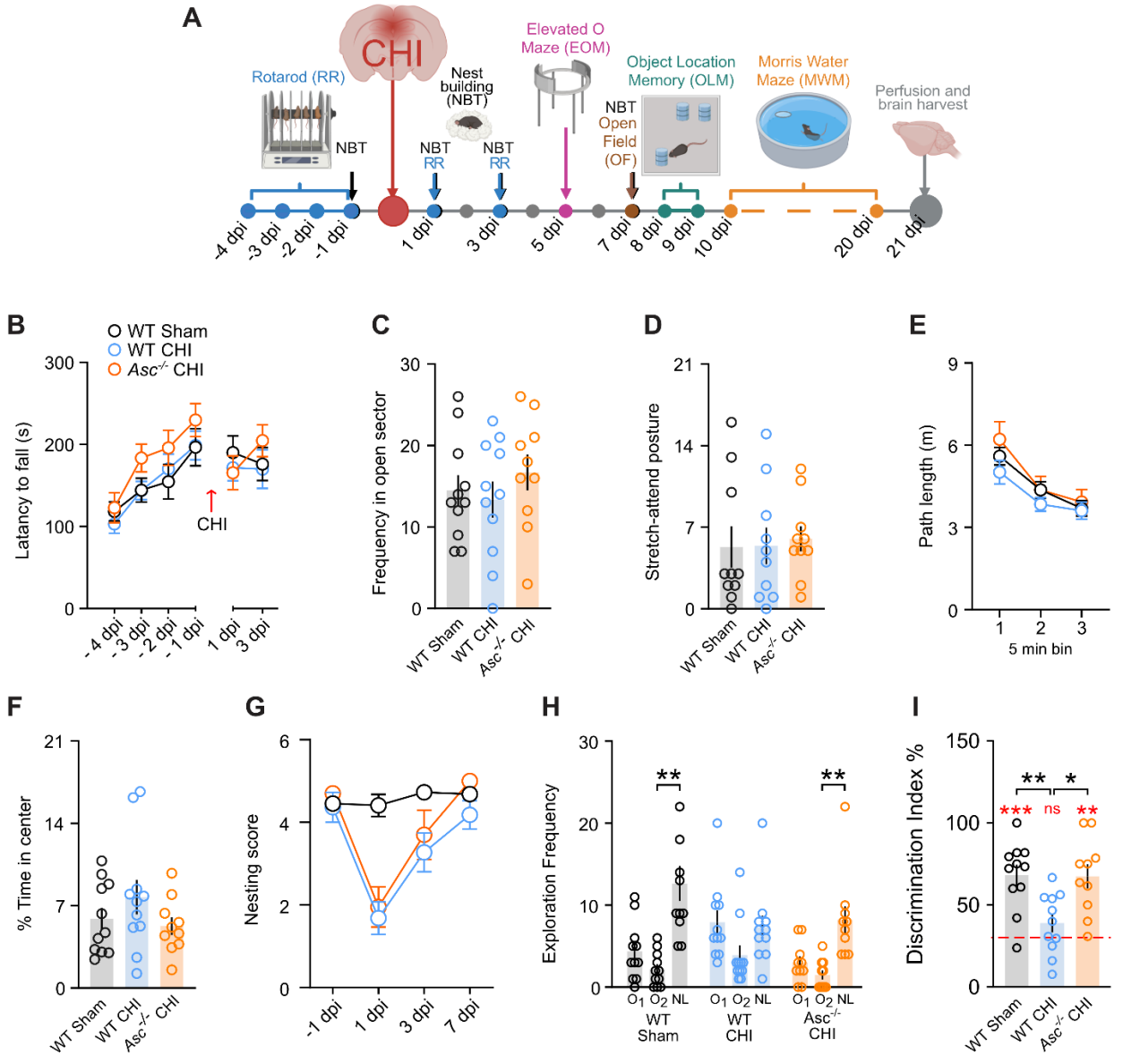

A. Experimental timeline of the behavioral test battery for cognitive assessment following CHI. Rotarod (RR) performance was evaluated between −4 and −1 days pre-injury and at 1- and 3 days post-injury (dpi). Nest building behavior (NBT) was assessed at −1, 1, 3, and 7 dpi. The elevated O-maze (EOM) was conducted at 5 dpi, the open field (OF) test at 7 dpi, the novel object location memory (OLM) test at 8 and 9 dpi, and the Morris water maze (MWM) from 10 to 20 dpi. **B–G.** Comparable behavioral performance among sham WT, CHI-injured WT, and CHI-injured *Asc*$^{-/-}$ mice in: (**B**) latency to fall during RR tests, (**C**) frequency in open sectors, (**D**) stretch-attend postures in the EOM, (**E**) path length, and (**F**) percentage of time spent in the center of the OF (n = 10-11 mice per genotype, one-way ANOVA), (**G**) NBT scores (n=10-11 mice per genotype, repeated measurements two-way ANOVA). **H–I.** CHI-injured *Asc*$^{-/-}$ mice, similar to sham WT

mice, (**H**) explored one of the displaced objects significantly more frequently than the other two (Friedman test with Dunn's multiple comparisons test **p < 0.01) and (**I**) exhibited a higher discrimination index compared with both the chance level (**p < 0.01, ***p < 0.001 by one sample t-test vs. 33.3% chance level in red dashed line) and CHI WT mice (*p < 0.05, **p < 0.01 by one-way ANOVA with Tukey's post hoc test).

Figure 6: Genetic deficiency of the Asc gene protects against mild cognitive deficits in the MWM following mild CHI.

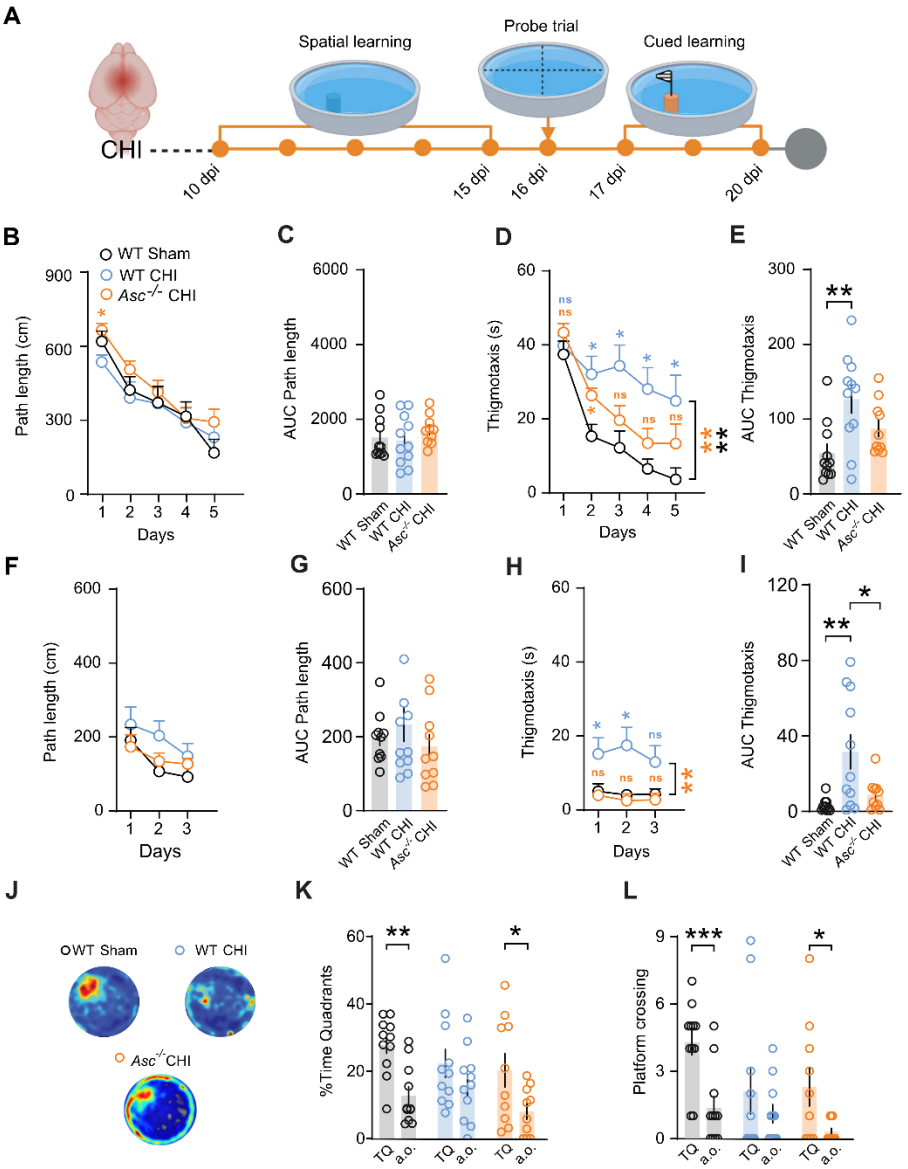

A. Experimental timeline for cognitive assessment following CHI, including spatial learning phase (10-15 dpi), probe trial (16 dpi), and cued learning (17-20 dpi) in the Morris water maze. **B-E.** Morris water maze performance in WT and *Asc*$^{-/-}$ mice, showing path length and thigmotaxis across spatial **B-E** and **F-J** cued training days (n = 10-11 mice per genotype *p < 0.05, **p < 0.01, ***p < 0.001, ****p < 0.0001 by repeated measurements two-way ANOVA with Tukey's post hoc test). Integrative AUC for path length and thigmotaxis from spatial learning (**C** and **E**) and cued learning phase (**G** and **I**). **J.** Representative heatmaps mean swimming trajectories and **K.** quantification of percentage of time spent in target in comparison to another quadrants (a.o.) or **L.** platform crossing times in virtual target platform in comparison to another virtual

platform (a.o.) (n =1 0-11 mice per genotype, *p < 0.05, **p < 0.01, ***p < 0.001 by ordinary one-way and two-way ANOVA with Tukey's post-hoc tests). Data are presented as mean ± SEM.

Figure 7. NLRP3 regulates ASC aggregation and distribution following CHI.

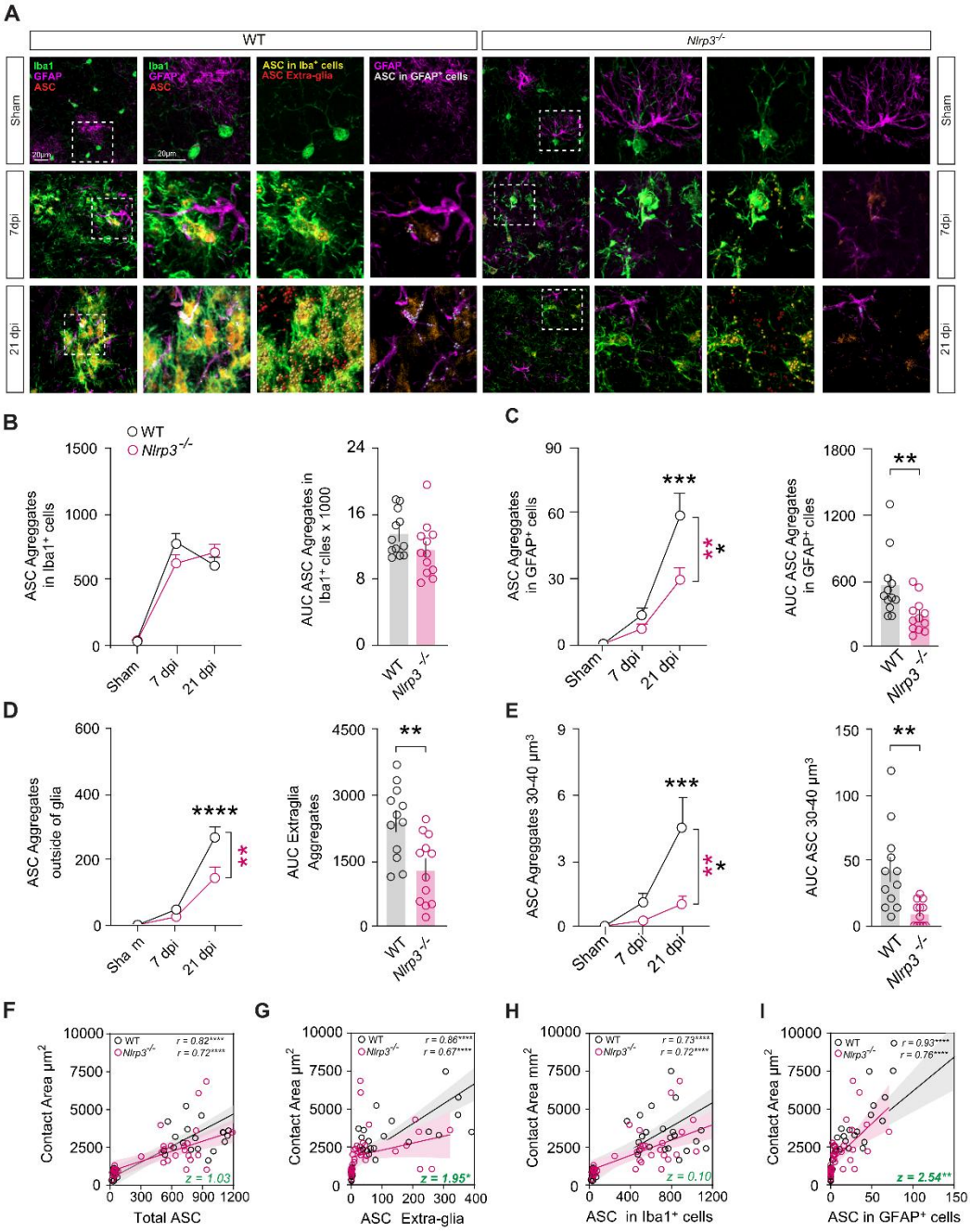

A. Immunohistochemistry for Iba1 (green), GFAP (magenta), and ASC (red) in cortices of WT and *Nlrp3*$^{-/-}$ mice at 7 and 21 dpi. ASC localizations within Iba1+ cells (yellow spots), GFAP^{+} cells (blue spots), and outside glial cells (red spots) were analyzed using IMARIS. Rectangles highlight examples of ASC distribution shown in high-magnification views. Scale bar, 20 μm. **B-E.** Quantification of total ASC aggregates numbers (**B**), intracellular ASC aggregates within Iba1^{+} cells (**C**), ASC aggregates outside glia cells (**D**), and ASC aggregates with a volume range 30–40 um^{3} (**E**) at 7 and 21 dpi in WT and *Nlrp3*$^{-/-}$ mice subjected to Sham or CHI. *n* = 12 slices from 4 mice per group per each time point, *p < 0.05, **p < 0.01,

915 ***$p < 0.001$, ****$p < 0.0001$ by ordinary two-way ANOVA with Bonferroni's post hoc test. Right panels show
916 integrative AUC of each marker over time (dpi). *$p < 0.05$, **$p < 0.01$, ***$p < 0.001$, ****$p < 0.0001$ by
917 Student's t-test. **F-I.** Spearman's correlation analysis (r) with a linear regression model (black lines WT, red
918 lines *Nlrp3*$^{-/-}$) with an interaction term for ASC aggregates (total, within glial cells, and outside glial cells) and
919 glia cell contact areas. n = 36 slices from 12 mice per genotype, *$p < 0.05$, **$p < 0.01$, ***$p < 0.001$, ****$p <$
920 0.0001. Differences between WT and *Nlrp3*$^{-/-}$ Spearman Correlation Coefficients (r) were performed using
921 the standard Fisher's z-transformation and subsequent comparison (87) *$p < 0.05$, **$p < 0.01$.
922

Supplemental data

Inflammasome adaptor ASC promotes sustained neuroinflammation and mild cognitive impairment in a closed-head injury model

Tao Li*[1], Sergio Castro-Gomez*#[1,2], Pablo Botella Lucena[3], Ana Vieira-Saecker[1], Stephanie Schwartz[1,2], Yingying Ding[2], Yushuang Deng[4], Maling Gou[5], Valentin Stein[2], Douglas T. Golenbock[6], Eicke Latz[7,8,9], Michael T. Heneka#[3,6]

1. Clinic of Parkinson, Sleep and Movement Disorders, Center for Neurology, University Hospital Bonn, University of Bonn, Bonn, Germany
2. Institute of Physiology II, University Hospital Bonn, University of Bonn, Bonn, Germany
3. Luxembourg Centre for Systems Biomedicine (LCSB), University of Luxembourg, Belvaux, Luxembourg
4. German Center for Neurodegenerative Diseases (DZNE), Bonn, Germany
5. Department of Biotherapy, Cancer Center and State Key Laboratory of Biotherapy, West China Hospital, Sichuan University, Chengdu, PR China
6. Division of Infectious Diseases and Immunology, University of Massachusetts Medical School, Worcester, USA
7. Institute of Innate Immunity, University Hospital Bonn, Bonn, Germany
8. Centre of Molecular Inflammation Research, Norwegian University of Science and Technology, Trondheim, Norway
9. Deutsches Rheuma-Forschungszentrum (DRFZ), Berlin, Germany

*__Authorship notes:__ TL and SC-G contributed equally to this work.

#__Correspondence__: michael.heneka@uni.lu, sergio.castro-gomez@ukbonn.de

__Competing interests:__ M.T.H. is a scientific advisory board member at Alector the Dementia Discovery Fund, and Muna Therapeutics and has received honoraria for oral presentations from Pfizer, Novartis, Roche, Abbvie, and Biogen. E.L. is a co-founder and adviser at IFM Therapeutics, Dioscure Therapeutics, Stealth' Biotech, and Odyssey Therapeutics.

Supplemental Figure 1: Single-Cell Transcriptomic Analysis of Brain Immune Cells Following TBI.

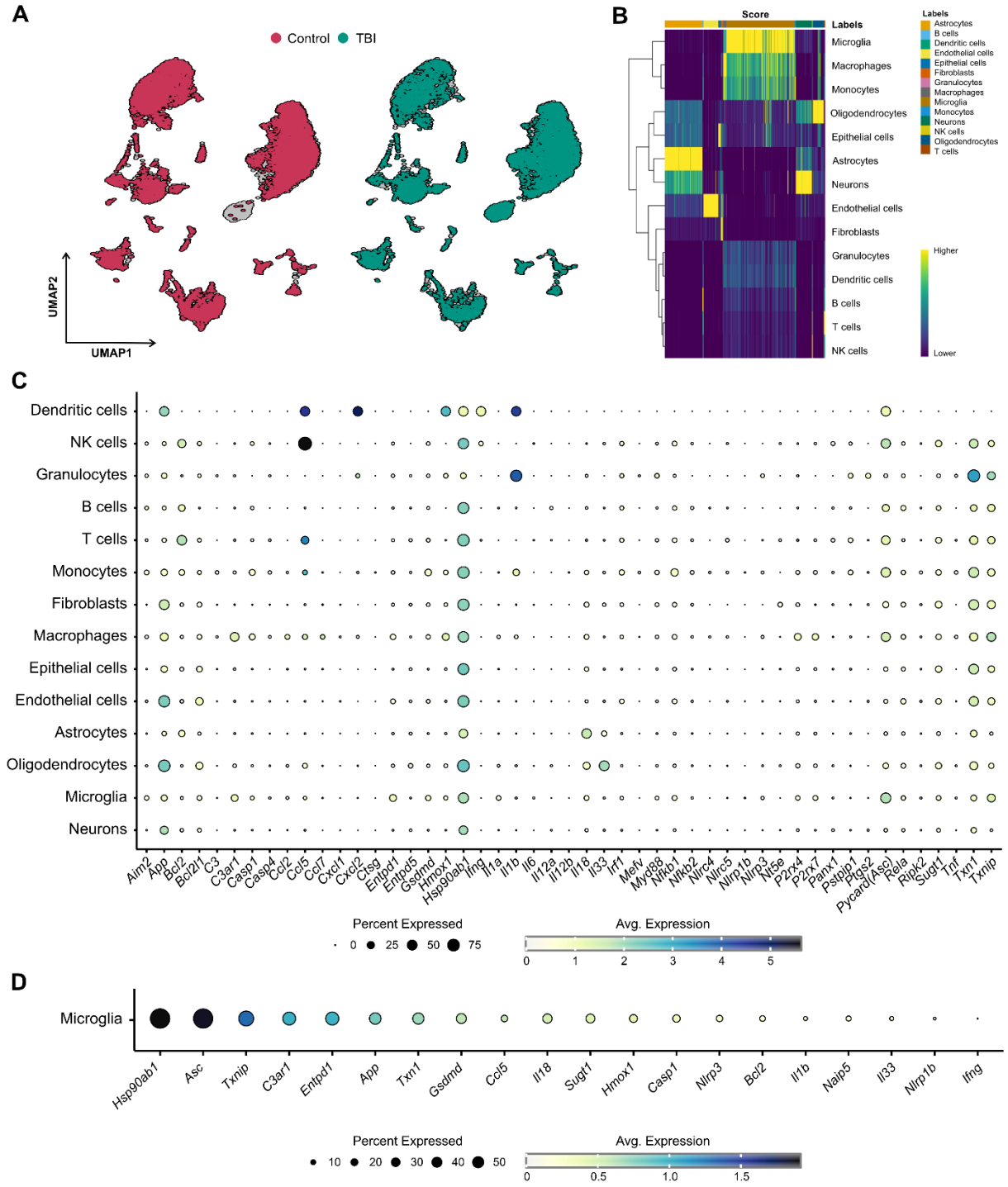

A. UMAP clustering of single-cell RNA sequencing (scRNA-seq) data, comparing control (red) and TBI (green) samples, illustrating shifts in immune cell populations post-TBI. **B.** Heatmap showing gene expression profiles across different brain cell types and cluster identification. **C.** Dot plot depicting the

expression of key inflammasome-related genes across different brain cell types. **D.** Dot plot depicting gene expression profile of inflammasome-related genes in microglia after TBI.

Supplemental Figure 2: ASC modulates expression and cleavage of CASP-8 and CASP-3 following CHI.

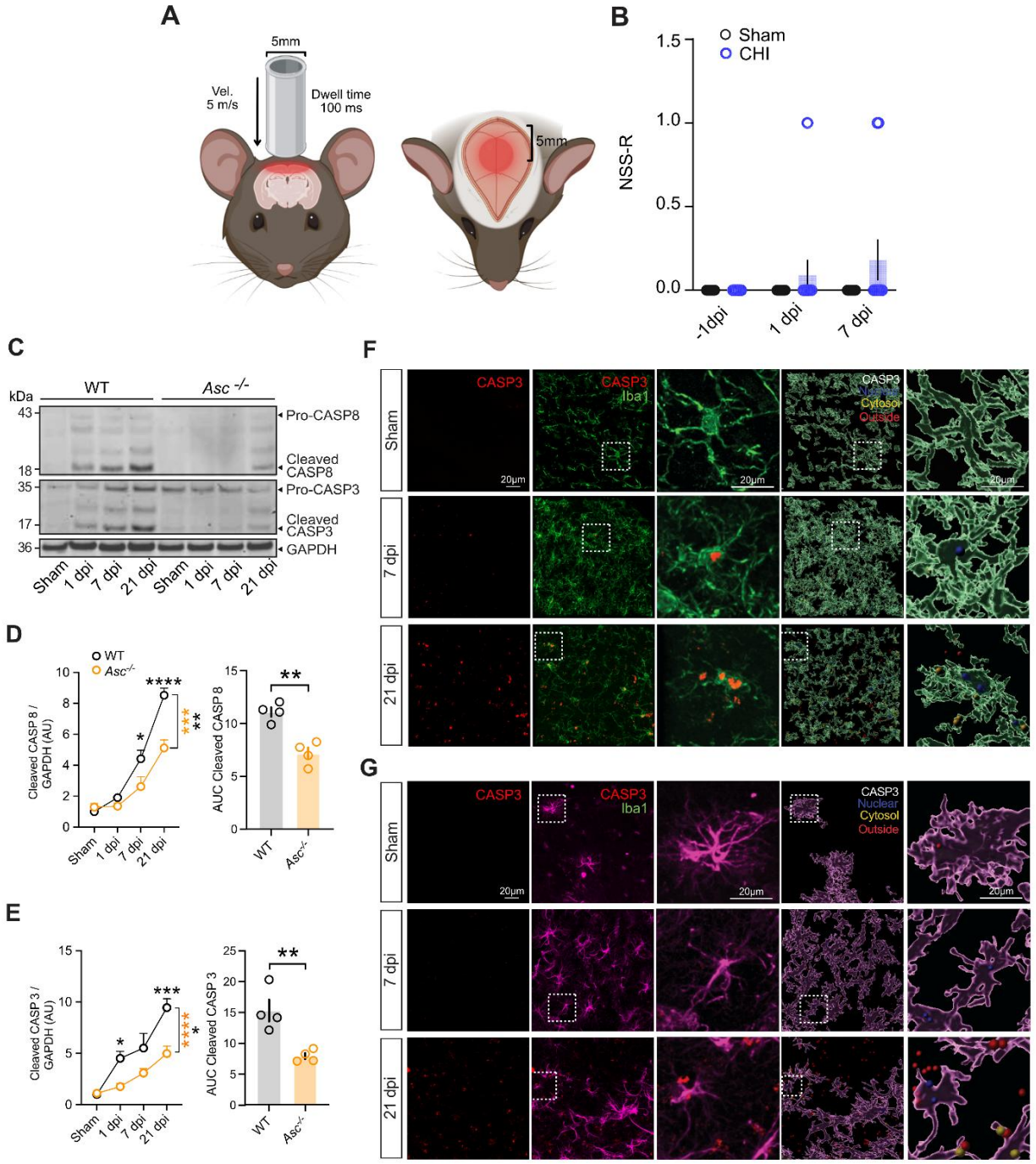

A. Schematic of injury model/location. Coronal view (right) shows tip positioned over the skull midline. Horizontal view (left) shows impact site relative to bregma. **B.** No significant motor, reflex or reaction deficits at 1- or 7-days post-intervention (dpi) when the mice were evaluated using the Revised Neurobehavioral Severity Scale (NSS-R). (Two-way ANOVA followed by Bonferroni's post-hoc tests, n = 11 mice per group per each time point, data are presented as the mean ± SEM)**. C.** Representative immunoblot images of

CASP 8 and CASP 3 at 1, 7, and 21 dpi in peri-contusional cortices of mice subjected to Sham or CHI, comparing WT and *Asc* $^{-/-}$ groups. **D-E.** Quantification of expressions of CASP 8 and CASP 3. The band intensity of a given target protein was normalized to the corresponding GAPDH signal for each sample. Data were further normalized to the average of the corresponding WT group and are presented as the mean ± SEM. Statistical significance was determined using two-way ANOVA followed by Bonferroni's post-hoc tests, n = 4 mice per group per each time point, *p < 0.05, **p < 0.01, ***p < 0.001, ****p < 0.0001 (left panels). Quantification of area under the curve (AUC) of each target over time (dpi) in WT and Asc$^{-/-}$ mice is shown in right panels. Statistical analysis was performed using an unpaired two-tailed t-test. Data are presented as the mean ± SEM. *p < 0.05, **p < 0.01, ***p < 0.001, ****p < 0.0001. **F–G**. Colocalization analysis of CASP3 immunoreactivity with Iba1^{+} and GFAP^{+} cells. Left panels show 3D reconstructions; blue dots indicate colocalization with the nuclear marker DAPI, yellow dots represent cytoplasmic localization, and red dots denote localization outside the cell.

Supplemental Figure 3: The cellular source of IL-1β following mTBI.

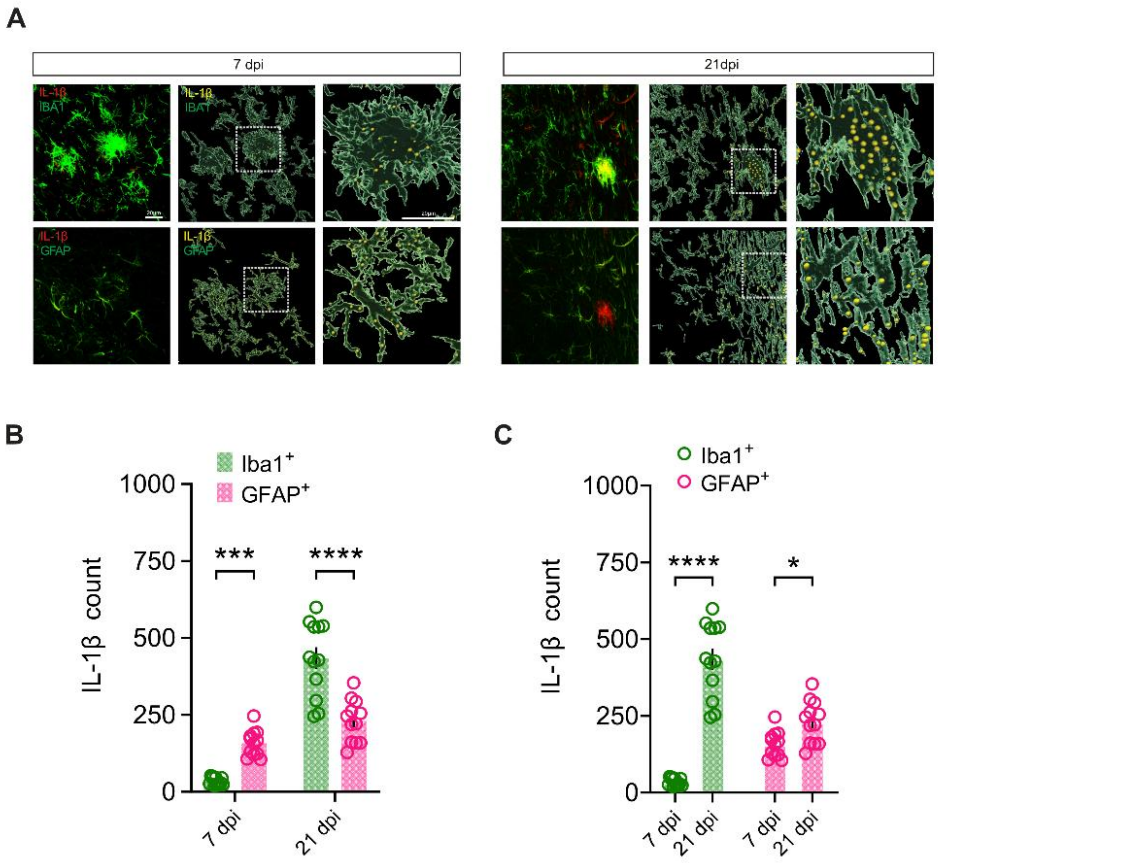

A. Representative images of immunohistochemical staining of the contusional cortices for IL-1β (red), Iba1 (green) and GFAP (green) in mice following sham surgery and 7 dpi and 21 dpi after CHI and 3D reconstruction of IL-1β immunostaining at 7 dpi and 21 dpi following CHI. IL-1β (yellow spots) localization within Iba1$^+$ and GFAP$^+$ cells. Scale bar, 20 μm. **B-C.** IL-1β spot counts assessed in Iba1$^+$ and GFAP$^+$ cells at 7 and 21 dpi following CHI. Data are presented as the mean ± SEM. Statistical significance was determined using two-way ANOVA followed by Bonferroni's post-hoc tests, n = 12 slices (4 mice) per group per each time point, *p < 0.05, **p < 0.01, ***p < 0.001, ****p < 0.0001.

Supplemental Figure 4: Mild Cognitive Impairment after CHI

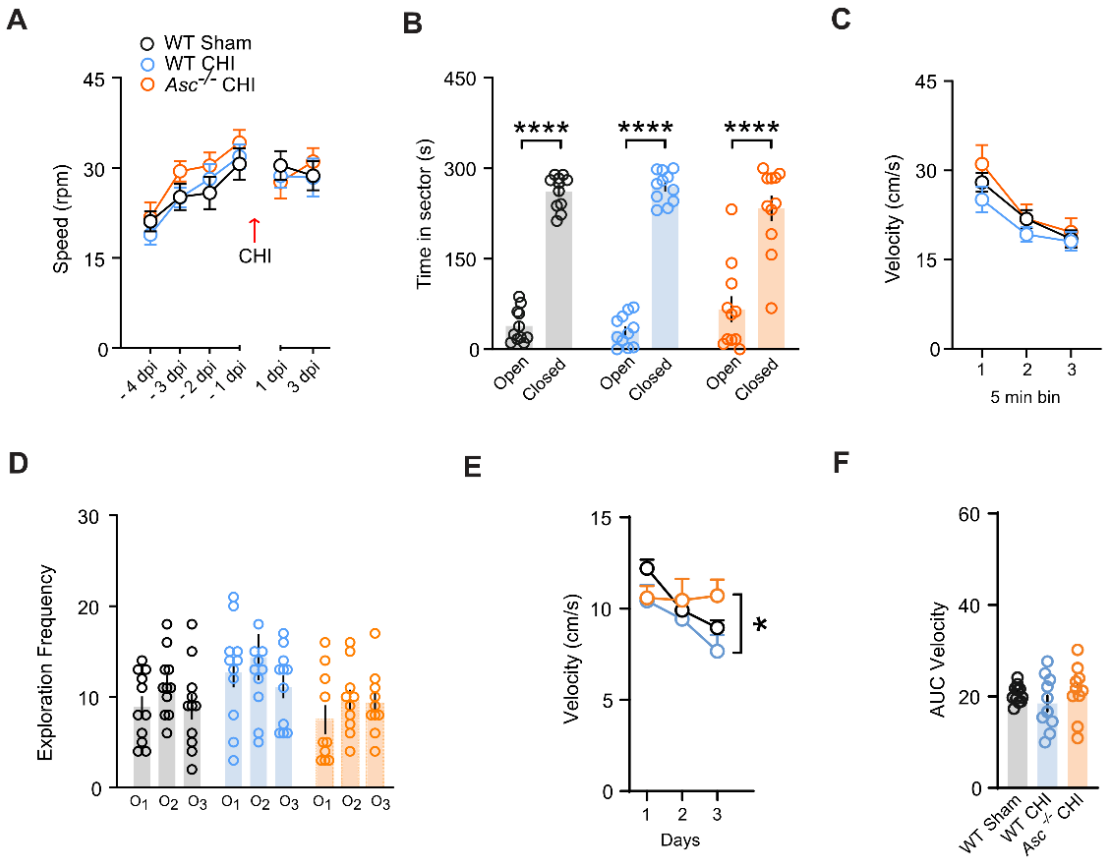

A. Rotarod performance, measured as falling speed, is comparable among WT Sham, WT CHI, and *Asc*$^{-/-}$ mice. **B**. WT Sham, WT CHI and *Asc*$^{-/-}$ mice spend significantly longer time exploring closed sectors compared to open sectors in the elevated O maze (EOM). **C**. Open field (OF) testing reveals similar locomotor velocities in WT Sham, WT CHI and *Asc*$^{-/-}$ mice. **D**. The frequency of exploration of the three identical objects is comparable across WT Sham, WT CHI and *Asc*$^{-/-}$ mice during the habituation phase of the Novel Object Location Memory test (OLM). **E**. Swimming velocity during cued learning in Sham WT, CHI-injured WT, and CHI-injured *Asc*$^{-/-}$. **F.** Comparison of the integrated area under the curve of swimming velocity. (n= 10-11 mice per genotype, *p < 0.05, **p < 0.01, ***p < 0.001 by ordinary one-way and two-way ANOVA with Tukey's post-hoc tests). Data are presented as mean ± SEM.

Supplemental Figure 5: ASC antibody validation and ASC aggregates analysis.

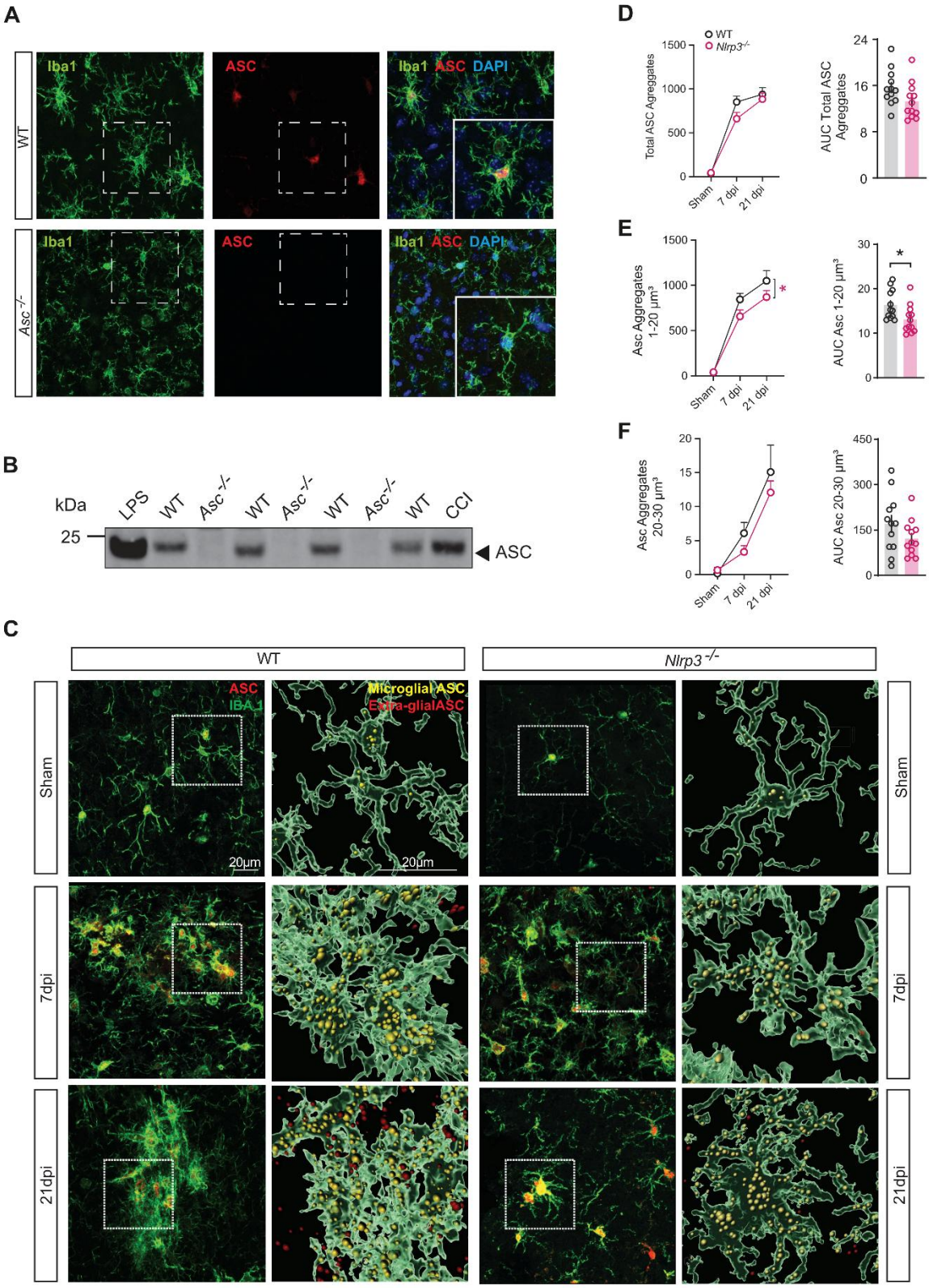

A-B. Validation of ASC antibody specificity using immunofluorescence staining and immunoblotting. **A.** ASC signal is detected in WT mice but absent in *Asc*$^{-/-}$ mice. **B.** Precipitated supernatant from LPS-stimulated primary microglia and cortical tissue from CCI brain-injured mice were used as positive controls. **C.** Representative immunohistochemical images of Iba1 (green) and ASC (red) in peri-contusional cortex of WT and *Nlrp3*$^{-/-}$ mice at different time points (sham, 7 dpi, 21 dpi). Same samples as Figure 7A. ASC aggregates were analyzed and 3D reconstructed using IMARIS. Scale bar, 20 µm. **D-F.** Quantification of ASC aggregation and ASC aggregates volume. Two-way ANOVA with Bonferroni's post-hoc tests (*$p < 0.05$, **$p < 0.01$, ***$p < 0.001$, ****$p < 0.0001$). n = 12 slices (4 mice) per group per each time point. Data are shown as mean ± SEM.